

An Interprocess Communication-based Two-way Coupling Approach for Implicit-Explicit Multiphysics Lattice Discrete Particle Model Simulations

Hao Yin* Matthew Troemner[†] Weixin Li* Erol Lale*
Lifu Yang[‡] Lei Shen[§] Mohammed Alnaggar[¶] Giovanni Di Luzio^{||}
Gianluca Cusatis**

September 13, 2024

*Northwestern University, Department of Civil and Environmental Engineering, Evanston, Illinois, 60208, United States

[†]North Fracture Group, Houghton, Michigan, 49931, United States

[‡]City University of Hong Kong, Department of Architecture and Civil Engineering, Hong Kong, 999077, China

[§]Hohai University, College of Water Conservancy and Hydropower Engineering, Nanjing, 210098, China

[¶]Oak Ridge National Laboratory, Oak Ridge, Tennessee, 37830, United States

^{||}Politecnico di Milano, Department of Civil and Environmental Engineering, Milan, 20121, Italy

**Corresponding author: g-cusatis@northwestern.edu

Abstract

In this study, the researchers have developed a Multiphysics-Lattice Discrete Particle Model (M-LDPM) framework that deals with coupled-fracture-poroflow problems. The M-LDPM framework uses two lattice systems, the LDPM tessellation and the Flow Lattice Element (FLE) network, to represent the heterogeneous internal structure of typical quasi-brittle materials like concrete and rocks, and to simulate the material's mechanical and transport behavior at the aggregate scale. The researchers revisited the LDPM governing equations and added the influence of fluid pore pressure. They also derived the Flow Lattice Model (FLM) governing equations for pore pressure flow through mass conservation balances for uncracked and cracked volumes. The M-LDPM framework was implemented using Abaqus user element subroutine VUEL for the explicit dynamic procedure of LDPM and user subroutine UEL for the implicit transient procedure of FLM. The coupling of the two models was achieved using Interprocess Communication (IPC) between Abaqus solvers. The M-LDPM framework can simulate the variation of permeability induced by fracturing processes by relating the transport properties of flow elements with local cracking behaviors. The researchers validated the M-LDPM framework by comparing the numerical simulation outcomes with analytical solutions of classical benchmarks in poromechanics.

Key words

Two-way coupling, Interprocess communication, Hydro-mechanical coupling, Lattice discrete particle model, Dual lattice

1 Introduction

Durability of materials for buildings and structures (e.g., concrete, stone, wood) is the result of a complex coupling of mechanics and multiphysical behaviors. While structures are suitably designed to consider strength criteria at the time of construction, the long-term behavior may not be appropriately predicted, resulting in additional material and economic costs, and often compounding the initial carbon emissions. It is, therefore, necessary to ensure design principles take into account the many factors which influence material durability to produce a structure with the optimal lifespan, and thus minimal environmental impact.

The interplay between fracture, mass transport, and heat transfer phenomena, is a widely studied multiphysics phenomenon. It has been studied by considering the internal structure of a multi-phase material and has attracted growing attention as it helps better understand the related phenomena. Previous experimental studies have shown that fracture permeability involves multiple physical processes, and is influenced by various factors such as fracture aperture and roughness [54, 57, 59], chemical precipitation and dissolution [17, 21], and thermal effects [46]. In particular, open and connected cracks have a strong influence on permeability. A large amount of previous work on fracture permeability has been conducted on prefractured (split or sawn) specimens and has shown that rock permeability is strongly related to density, spacing, orientation, width, and length of fractures within specimens [12, 15, 28]. However, researchers suggested that permeability studies of rocks fractured at in situ conditions through triaxial compression or direct shear tests can better represent fracture properties in the subsurface than prefractioned or artificial specimens [10, 23, 32, 41, 49]. Indeed, some factors such as the influence of stress state during fracture, the transition from brittle to ductile failure, effective stress and hysteresis effects can be only investigated under in situ conditions.

Furthermore, simulating the fluid transport and hydro-mechanical coupling effect at different

length scales is possible. At the microscopic level, fluid flow can be solved by using Navier-Stokes equations with certain assumptions. The hydro-mechanical coupling effect can also be captured through force-based interaction across the fluid-solid interface [11,44]. However, this approach requires knowledge of the pore network structure and high computational resources. An alternative to the costly microscopic approach is a mesoscopic/macrosopic approach [8,27,31,35,53] which adopts diffusion equations to describe fluid flow in a porous medium and relies on phenomenological laws such as Darcy’s law, Fick’s law, and lubrication theory. By introducing diffusion coefficients, such as hydraulic conductivity, permeability, and diffusivity in the sense of homogenization over the multi-phase mixture [19, 20], this approach benefits from affordable computational cost. The flow solver and length scale choice involves a trade-off between physical accuracy and computational cost.

This work develops a numerical framework called the Multiphysics Lattice Discrete Particle Model (M-LDPM) to study the two-way coupling behavior of porous flow and fracture permeability of quasi-brittle materials in three-dimensional (3D) simulations. The M-LDPM framework has been verified by simulating various classical benchmark examples, including 1D Terzaghi’s consolidation and hydraulic fracturing. The proposed model falls in the broader category of discrete models formulated to simulate material heterogeneity [7,11,27,31,40,55] and its effect on fracturing behavior, which in turn is crucial to predict materials fracture permeability. This study has two major objectives: (1) to provide a solid theoretical and computational framework to investigate the correlation between cracking and flow events on a small scale (tens of microns) with the response of laboratory specimens on a greater scale (millimeters to centimeters); (2) to help interpret the results of complex fracture permeability laboratory experiments. It is important to note that although the model is suitable for field-level use along with applications that represent large-scale features like rock joints and faults, appropriate multiscale techniques are required for those applications, and this paper focuses solely on the objectives previously mentioned.

2 Lattice Discrete Particle Model (LDPM) for multi-physics analyses

2.1 Topologically dual systems of lattice models

Lattice models of solids have been motivated, in large part, by the discontinuous and heterogeneous nature of material structure and its breakdown under external loading. These models have been extensively developed over the past few decades, enabling researchers to study the material structure-property relationships in new and innovative ways. Furthermore, lattice models are now being extended to include additional physical, chemical, or biological processes to ensure the material's durability and sustainability under rapidly changing environmental conditions.

Discretization of the material domain plays a crucial role in the representation of mechanical or transport behaviors in the presence of material heterogeneity. Among the various discretization techniques, the most promising method is one that naturally captures the intrinsic geometric properties of material internal structure (e.g., heterogeneity, anisotropy) while also possessing a topologically dual geometric system. One of the most famous examples of the topologically dual systems is the Voronoi-Delaunay dual graph [18].

This duality is particularly important to lattice models. Many lattice models use Voronoi and/or Delaunay diagrams for geometric characterization to achieve unbiased spatial discretization and to capture the intrinsic heterogeneous structure of the material. If one of these geometric structures is employed for spatial discretization, the duality provides a naturally coupled spatial discretization for the void or different phase of material within the same model domain. This facilitates multi-field analysis with strong coupling between different phases.

The dual graph approaches have been widely adopted in subjects such as physics, chemical engineering, biological engineering, and material sciences in the past several decades [1, 2, 9, 29, 37, 42, 51]. In poromechanics, the work of Grassl [25] introduced the concept of a dual lattice with aligned cracks and conduit elements, allowing for an accurate reflection of the crack opening effect on the flow. The dual lattice approach was later extended to 3D [26]. Several other papers have employed this concept, e.g., for simulating cracking due to rebar corrosion [22] and hydraulic fracturing [3, 4, 50]. Li et al. [36] have applied the dual lattice concept to shale fractures by adding effects of mechanical volumetric strain rate on pressure. Shen et al. [47, 48] have used the dual lattice concept to accurately simulate concrete thermal spalling and multiaxial load-induced thermal strain at high temperatures. Yang et al. [55, 56] have simulated volumetric strain and cracking in concrete induced by alkali-silica reaction within the dual lattice framework.

2.2 LDPM under multiphysics context

A typical usage of topologically dual lattice systems is the Multiphysics-Lattice Discrete Particle Model (M-LDPM) for the multiscale multiphysics analysis of granular-dominant quasi-brittle materials (e.g., concrete, rock). M-LDPM is formulated in a discrete poromechanics setting by adopting two coupled dual lattices simulating mechanical and transport behaviors, respectively. The model adopts an “a priori” discretization of the internal structure of the material at the mesoscale, which is the length scale of major material heterogeneities.

2.2.1 LDPM basis

Originally proposed by Cusatis et al. [13, 14], the Lattice Particle Discrete Model (LDPM) cell system provides a geometrical characterization for fracture behaviors of concrete, and then extended to other quasi-brittle materials [36, 39]. To capture the granular nature of the in-

ternal mesostructure, LDPM tessellates the model domain with randomly packed polyhedral cells, which represent the volumes of cementitious fine mortar surrounding coarse aggregate particles. Figure. 1 briefly illustrates the construction of LDPM “particle-facet-cell” system and its topologically dual Flow Lattice Model (FLM) network [58], which provides the geometrical characterization of the flow (transport) behaviors of the material. It is proposed to be more reflective of the tortuosity of the flow path (so-called “heterogeneity” of the 3D flow network) in the matrix phase of the cementitious materials. When cracks appear, the crack openings at the LDPM facets will cause the growth in the permeability/conductivity of the material. Such a coupling with the cracking behavior is one of the key features of the FLM, as a part of the M-LDPM framework.

2.2.2 Dual graph of LDPM tessellation

The construction of LDPM cell system can be illustrated as follows:

- (i) Non-overlapped spherical particles are randomly placed from the largest to the smallest size in the model domain as the idealized aggregates or rock grains (see Fig. 1a). The size distribution of the spherical particles can follow a grain size curve, e.g., Fuller curve for concrete [24]. Detailed placation algorithm can be found in [14].
- (ii) A constrained Delaunay tetrahedralization connects the particle centers and creates tetrahedra (called LDPM tetrahedra) that tessellate the model domain. Within each LDPM tetrahedron, a facet system is formulated: (1) edge points are defined at midways of the edges belonging to the associated particles (e.g., E_{12} for P_1 and P_2 in Fig. 1b); (2) face-points are defined in association with a triangular face formulated with three adjacent particles. For each face of the tetrahedron, the corresponding face-point must be located at the connection of the particle center and the edge-point belonging to the edge opposite to that particle (e.g., F_4 for face $P_1P_2P_3$ must be located at the connection of E_{12} and P_3 in Fig. 1b); (3)

similarly, the tet-points are defined as the midways identified on the straight lines connecting face-points of the tetrahedra and the fourth particles, which are opposite to the face-points (e.g., tet-point N for tetrahedron $P_1P_2P_3P_4$ must be located at the connection of F_4 and P_4 in Fig. 1b). By formulating triangular facets with vertices consisting of one tet-point, one edge-point, and one face-point, 12 facets (also called LDPM facets, see Fig. 1c) in total can be formulated within each LDPM tetrahedron. Facets belonging to adjacent LDPM tetrahedra surround particles and tessellate the model volume into a system of polyhedral cells (Fig. 1d, e, and f). This 3D domain tessellation is anchored to the Delaunay tetrahedralization but does not exactly coincide with the classical Voronoi tessellation. The LDPM facets describe the potential crack locations in section 3. As often verified in practice, cracks occur at the grain interface and in the embedding matrix as opposed to cutting through grains.

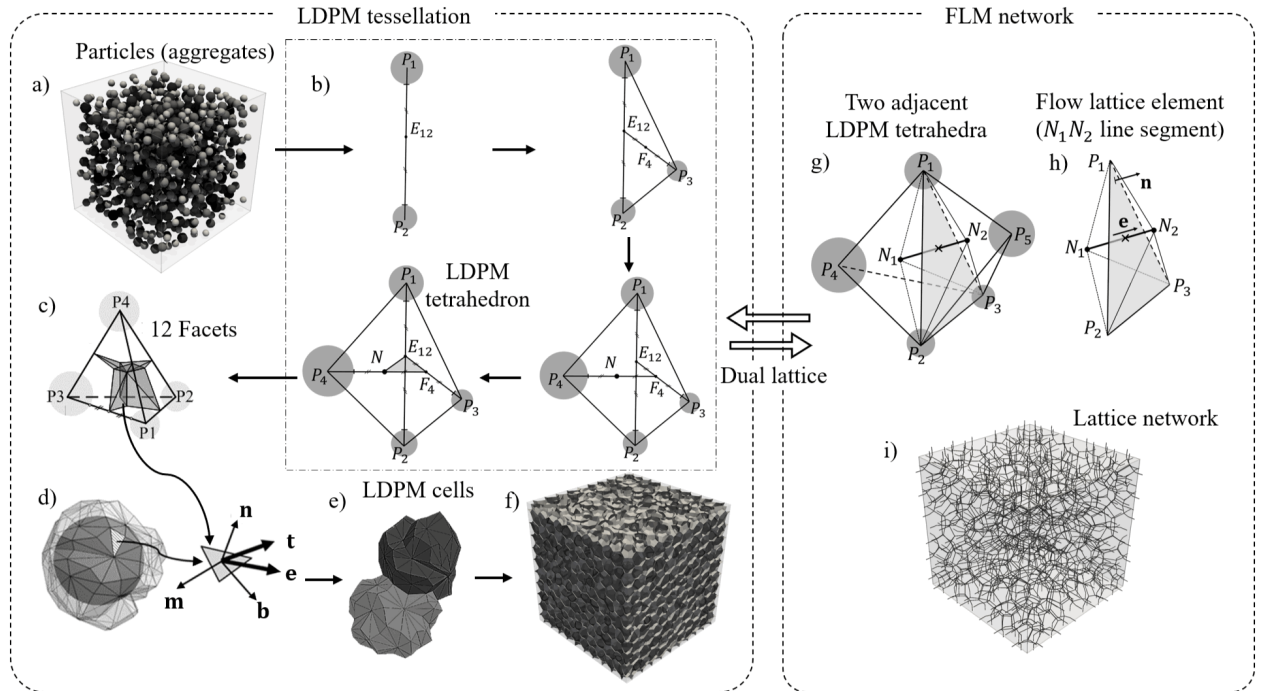


Figure 1: Topologically dual lattice of LDPM tessellation, modified from [58]

(iii) As the dual graph of the LDPM tessellation, a flow lattice network can be formed by connecting the tet points belonging to each pair of two adjacent LDPM tetrahedra with 1D line transport elements, the resulting network is shown on the right of Fig. 1. At the

mesoscale level, the scale of the major heterogeneity of the material (coarse aggregate particles), two phenomena are explicitly accounted by the flow lattice network for (a) the tortuosity of the flow path that is preferentially located in the mortar between adjacent coarse aggregate particles; and (b) the effect of cracking that increase permeability/conductivity. As introduced in the next section, the dual lattice topology enables the seamless coupling of the fracture and flow behavior.

It would be important to notice that the current model does not have the resolution to account for some smaller-scale physical phenomena. Taking concrete at the microscopic level as an example, the influence of the Interfacial Transition Zone (ITZ) must be considered. The ITZ, which is approximately 100 microns around each aggregate particle, exhibits a porosity that is about 40% higher than that of the cement paste. To account for this effect the model would need to be formulated at a smaller length scale. This is beyond the scope of this paper.

3 Coupling of poroflow and cracking behaviors

The mechanical and flow behaviors of the material are modeled with the M-LDPM governing equations, in the following section, the mechanical part and the flow part of M-LDPM governing equations are formulated in two numerical algorithms, the derived matrix forms are also presented. The coupling mechanisms are highlighted and can be then implemented for practical applications, as introduced in section 4.

3.1 Governing equations

LDPM Kinematics and Constitutive Laws

The LDPM formulation [14] is briefly reviewed first. In the LDPM formulation, adjacent cells

interact through shared triangular facets (see Fig. 1d). Rigid-body kinematics is adopted to describe the heterogeneous deformation of the cell system. Three strain measures, one normal component and two shear components, are defined at each facet as:

$$e_N = \frac{1}{\ell} \mathbf{n}^T \cdot [\![\mathbf{u}_C]\!]; \quad e_M = \frac{1}{\ell} \mathbf{m}^T \cdot [\![\mathbf{u}_C]\!]; \quad e_B = \frac{1}{\ell} \mathbf{b}^T \cdot [\![\mathbf{u}_C]\!] \quad (1)$$

where $[\![\mathbf{u}_C]\!]$ is the displacement jump vector calculated by the displacements and rotations of the nodes adjacent to the selected facet; ℓ = tetrahedron edge associated with the facet; \mathbf{n} is a unit vector normal to each facet, and \mathbf{m} and \mathbf{b} are two mutually orthogonal unit vectors contained in a plane orthogonal to \mathbf{n} .

The facet stress vector applied to the solid phase, $\mathbf{t} = t_N \mathbf{n} + t_M \mathbf{m} + t_B \mathbf{b}$, is calculated through appropriate constitutive laws, which describes various phenomena of the solid grain interaction (Fig. 1e and f).

In the elastic regime, the mechanical facet stress components are proportional to the corresponding strain components:

$$\mathbf{t} = \begin{bmatrix} t_N \\ t_M \\ t_B \end{bmatrix} = \begin{bmatrix} E_N & 0 & 0 \\ 0 & E_M & 0 \\ 0 & 0 & E_B \end{bmatrix} \begin{bmatrix} e_N \\ e_M \\ e_B \end{bmatrix} \quad (2)$$

where $E_N = E_0$ is the normal modulus, $E_M = E_B = \alpha E_0$ is the shear modulus, and α = normal-shear coupling coefficient. Beyond the elastic limit, the vectorial constitutive laws are formulated to reproduce three distinct nonlinear phenomena. The first source of nonlinearity is related to fracturing and cohesive behavior under tension for $e_N > 0$. Following the work of Cusatis et al. [14], one can define effective strain and effective stress as $e = [e_N^2 + \alpha (e_M^2 + e_B^2)]^{1/2}$, $t = [t_N^2 + (t_M^2 + t_B^2) / \alpha]^{1/2}$, respectively, and compute the normal and shear stresses as: $t_N = e_N(t/e)$, $t_M = e_M(t/e)$, $t_B = e_B(t/e)$. The effective stress t is

incrementally elastic ($\dot{t} = E_0 \dot{e}$) and must satisfy the inequality $0 \leq t \leq \sigma_{bt}(e, \omega)$, in which:

$$\sigma_{bt} = \sigma_0(\omega) \exp [-H_0(\omega) \langle e_{\max} - e_0(\omega) \rangle / \sigma_0(\omega)] \quad (3)$$

where the Macaulay bracket defines: $\langle x \rangle = \max(x, 0)$, and ω is defined as: $\tan \omega = e_N / \sqrt{\alpha(e_M^2 + e_B^2)}$. The function $\sigma_0(\omega)$ represents the strength limit for the effective stress with a smooth transition between pure tension ($\omega = \pi/2$) and pure shear ($\omega = 0$), and is given by:

$$\sigma_0(\omega) = \sigma_t \frac{-\sin(\omega) + \sqrt{\sin^2(\omega) + 4\alpha \cos^2(\omega)r_{st}^2}}{2\alpha \cos^2(\omega)r_{st}^2} \quad (4)$$

where $r_{st} = \sigma_s/\sigma_t$ is the ratio between the mesoscale shear strength (or cohesion) σ_s and the mesoscale tensile strength σ_t . After the maximum effective strain reaches its elastic limit $e_0(\omega) = \sigma_0/E_0$, the stress boundary σ_{bt} decays exponentially with a softening modulus, $H_0(\omega) = H_s/\alpha + (H_t - H_s/\alpha)(2\omega/\pi)^{nt}$, which provides a smooth transition from softening behavior under pure tension $H_0 = H_t$, to perfectly plastic behavior under pure shear $H_0 = 0$. For the correct energy dissipation during mesoscale damage localization to be preserved, the softening modulus in pure tension is expressed as $H_t = 2E_0 / (\ell_t/\ell - 1)$, where $\ell_t = 2E_0 G_t / \sigma_t^2$ is the characteristic length, G_t is the mesoscale fracture energy, and ℓ is the length of the tetrahedron edge (mechanical lattice element) associated with the facet.

Since relevant to the effect of cracking on permeability discussed later, it is worth pointing out that the mesoscale crack opening components (normal and shear) can be calculated as:

$$\delta_i = \ell (e_i - t_i/E_i) \quad (i = N, M, B) \quad (5)$$

The second source of nonlinearity is from pore collapse and material compaction. For compressive condition $e_N < 0$, the effective stress is again incrementally elastic, and is constrained by the strain-dependent stress boundary, $-\sigma_{bc}(e_D, e_V) \leq t \leq 0$, in which e_V is the volumetric

strain, and e_D is the deviatoric strain. The strain-dependent stress boundary is modeled by an exponential evolution for pore collapse, compaction, and re-hardening as illustrated by:

$$\sigma_{bc} = \begin{cases} \sigma_{c0} & -e_V \leq 0 \\ \sigma_{c0} + \langle -e_V - e_{c0} \rangle H_c(r_{DV}) & -e_V \leq e_{c1} \\ \sigma_{c1}(r_{DV}) \exp [(-e_V - e_{c1}) H_c(r_{DV}) / \sigma_{c1}(r_{DV})] & -e_V > e_{c1} \end{cases} \quad (6)$$

where $r_{DV} = |e_D|/e_V$ for $e_V > 0$ and $r_{DV} = -|e_D|/(e_V - e_{V0})$ for $e_V \leq 0$ in which $e_{V0} = \kappa_{c3} e_{c0} \cdot e_{c0} = \sigma_{c0}/\sigma_{c1}$ is the volumetric strain at the onset of pore collapse, σ_{c0} is the mesoscale yielding compressive stress, $e_{c1} = \kappa_{co} e_{c0}$ is the strain at which the rehardening starts. κ_{c0} and κ_{c3} are material parameters. $\sigma_{c1}(r_{DV}) = \sigma_{c0} + (e_{c1} - e_{c0}) H_c(r_{DV})$ in which $H_c(r_{DV})$ is defined as $H_c(r_{DV}) = H_{c1} + (H_{c0} - H_{c1}) / (1 + \kappa_{c2} (r_{DV} - k_{c1}))$ where $H_{c0}, H_{c1}, \kappa_{c1}$ and κ_{c2} are material parameters.

The third source of nonlinearity is related to frictional behavior under compression. This can be simulated effectively through a non-associative incremental plasticity formulation in which, during plastic flow, $\varphi(t_N, t_M, t_B) = 0$, the incremental shear stresses are computed as $\dot{t}_M = E_M (\dot{e}_M - \dot{e}_M^P)$, $\dot{t}_B = E_B (\dot{e}_B - \dot{e}_B^P)$ and the normal stress is simply elastic $\dot{t}_N = E_N \dot{e}_N$. In the previous expressions, $\varphi(t_N, t_M, t_B)$ is the yielding function, $e_M^P = \dot{\lambda} \partial \psi / \partial t_M$ and $e_B^P = \dot{\lambda} \partial \psi / \partial t_B$ are the shear plastic strain increments, and λ is the plastic multiplier, $\psi = \psi_0 (t_M^2 + t_B^2)^{1/2}$ is the plastic potential. The yielding function can be formulated according to a Mohr-Coulomb criterion as

$$\varphi = (t_M^2 + t_B^2)^{1/2} - \sigma_s + \mu_0 t_N \quad (7)$$

in which μ_0 is the internal friction coefficient.

The facet stresses calculated through the constitutive laws described above represent the

stresses carried by the solid phase. Equilibrium considerations at the facet level allow for the reasonable assumption of a parallel coupling between the stresses carried by the solid phase and those by the fluid phase. In this work, the effective stress concept from Biot's theory of poroelasticity [5] is adopted, and the total stress vector on each facet can be computed as

$$\mathbf{t}^{\text{total}} = \mathbf{t} - b\mathbf{t}^{\text{eigen}} \quad (8)$$

where b is the Biot coefficient, and $\mathbf{t}^{\text{eigen}} = p\mathbf{n}$, p is the magnitude of effective pore pressure of fluid. The negative sign in Eq. 8 comes from the pressure sign convention, which is positive for the fluid and negative for the solid.

Equilibrium

The equilibrium is obtained through the linear and angular momentum balance equations of each polyhedral cell subjected to the force resultants obtained by multiplying the tractions in Eq. 8 times the facet areas for all facets belonging to the given cell, one can write:

$$\sum_{k \in \mathcal{F}_I} A_k \mathbf{t}_k^{\text{total}} + V^I \mathbf{b} = \mathbf{M}_u^I \ddot{\mathbf{u}}_I + \mathbf{M}_\varphi^I \ddot{\boldsymbol{\varphi}}_I \quad (9)$$

$$\sum_{k \in \mathcal{F}_I} A_k \mathbf{c}_k^I \times \mathbf{t}_k^{\text{total}} + V^I \mathbf{a}^I \times \mathbf{b} = \mathbf{I}_u^I \ddot{\mathbf{u}}_I + \mathbf{I}_\varphi^I \ddot{\boldsymbol{\varphi}}_I \quad (10)$$

where \mathcal{F}_I is the set of facets surrounding the node P_I (located inside cell I); A_k is the projected area of k -th facet orthogonal to the corresponding tetrahedron edge, V^I is the cell volume, \mathbf{c}_k^I is the distance between facet centroid and particle center, \mathbf{a}^I is the distance between the cell centroid and the particle center, \mathbf{b}^I is the external body force, \mathbf{t}_k is the stress traction vector, \mathbf{M}_i^I and \mathbf{I}_i^I ($i = u, \varphi$) are inertia matrices, and \mathbf{u}_I and $\boldsymbol{\varphi}_I$ are displacement and rotation vectors, respectively. In the current implementation, an explicit dynamic algorithm (based on a central difference scheme) is adopted to solve the equations above by a quasi-static method (i.e., small loading rate) and to simulate the static mechanical behavior. This offers the advantage of avoiding the convergence problems that implicit schemes often

encounter in handling softening behaviors.

Discrete Formulation of Fluid Flow

This section discusses the formulation of flow phenomena in the Flow Lattice Element (FLE) system, a discrete topologically dual with the LDPM. Following Li et al. [36], the formulation of FLE applies to the fluid flow under full saturation conditions, constant room temperature, and assuming that fluid behaves as a slightly compressible Newtonian fluid. According to the settings depicted in [58], each FLE connects the centroids of two adjacent LDPM tetrahedra in the undeformed configuration: named tet $P_1P_2P_3P_4$ and tet $P_1P_2P_3P_5$ (Fig. 2a). The two adjacent LDPM tetrahedra have a common triangular face A_0 with a normal \mathbf{n} , across which an FLE connects the tetpoints N_1 and N_2 located inside the two tetrahedra. A directional vector \mathbf{e} orienting from N_1 to N_2 represents the flow direction in the FLE. The FLE is associated to two pyramidal volumes, V_1 and V_2 , identified by the points P_1, P_2, P_3, N_1 and P_1, P_2, P_3, N_2 . The volumes can be computed as $V_i = Al_i/3$ ($i = 1, 2$), where $A = |\mathbf{n} \cdot \mathbf{e}|A_0$ is the projected area of triangular cross-section $P_1P_2P_3$ (A_0) in the direction \mathbf{e} ; the segment lengths l_i are associated with the total length of FLE l , which intersects the cross-section $P_1P_2P_3$ (A_0), one can define the length proportionality coefficients which satisfy the relations $g_i = l_i/l$ ($i = 1, 2$).

The direct coupling between the mechanical model and the flow model lays in the information of the local crack openings of six sub-parallel LDPM facets, with respect to the flow direction \mathbf{e} , i.e., δ_{Nj}^i ($j = 1, 2, 3$) associated with V_i ($i = 1, 2$) in Fig. 2b, which is updated by the mechanical model. These sub-parallel LDPM facets have the areas A_{fj}^i (Fig. 2c) and the inspection lines of facets on either side V_1 or V_2 with the triangular face A_0 have the lengths of l_{fj} .

Fluid Flux for Uncracked Material

The mass of fluid in the uncracked control volume V_i ($i = 1, 2$) can be written as $M_{fu}^i = m_{fi}V_i$

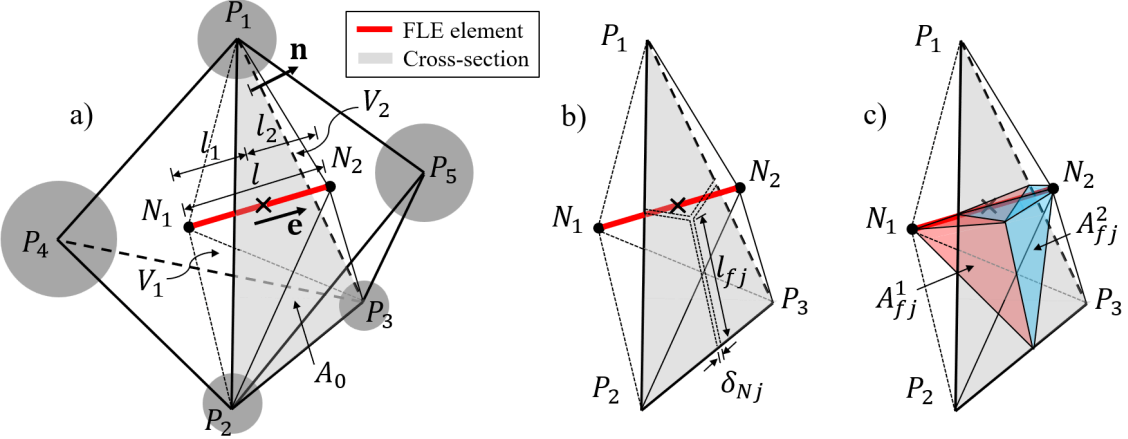


Figure 2: Diagrams of the Flow lattice element (FLE): a) FLE geometry, b) the associated LDPM facets; c) the cracked triangle face and the illustration of normal crack opening;

in which m_{fi} is the fluid mass content, defined to be the fluid mass per unit reference volume. The change in fluid mass content can be related to the increment of fluid content $\zeta_i = (m_{fi} - m_{f0}) / \rho_{f0}$, where m_{f0} and ρ_{f0} are fluid mass content and density in the reference state, respectively. For slightly compressible fluids, the fluid density in the current state can be related to ρ_{f0} by defining the bulk modulus K_f ; one can write $\rho_{fi} = \rho_{f0} [1 + (p_i - p_0)/K_f]$ ($i = 1, 2$), where p_i is the current fluid pressure in V_i , and p_0 is the initial/reference pressure.

According to the classic theory of poromechanics [5, 43], the increment of fluid content, ζ_i , can be expressed as a linear combination of the volumetric strain, e_{vi} , of the solid phase defined as the relative variation of the solid volume, and the fluid pressure, p_i , as $\zeta_i = b e_{vi} + p_i/M_b$, where M_b denotes the Biot modulus (also defined as the reciprocal of the so-called storage coefficient). It is worth pointing out that b and M_b may vary due to material heterogeneity. The effect of this variation is insignificant in the context of this paper and will be neglected thereafter. Also, the previous discussion on b and its evolution with damage also holds for M_b . Again, in absence of relevant experimental data, a constant value is actually used in this paper.

One can write the time variation of the fluid mass in the control volume V_i ($i = 1, 2$) as:

$$\dot{M}_{fu}^i = \rho_{f0} \left(b\dot{e}_{vi} + \frac{\dot{p}_i}{M_b} \right) V_i \quad (11)$$

The mass flux through the uncracked area A from V_1 into V_2 reads $Q_{fu} = Aj_p$, the flux density j_p can be obtained by using Darcy's law, which can be written as:

$$j_p = -\bar{\rho}_f \frac{\kappa_0}{\mu_f} g_p \quad (12)$$

where κ_0 and μ_f denote the intrinsic permeability of the material and the fluid viscosity, respectively, $\bar{\rho}_f = g_2\rho_{f1} + g_1\rho_{f2}$ is an estimate of the weighted average density of fluid in the volume V , and g_p is the discrete estimation of pore pressure gradient from V_1 into V_2 .

Fluid Flux for Cracked Material

The influence of cracks on the FLE can be considered in two parts: (1) the fluid mass stored in the cracked volumes, and (2) the fluid flux through the cracked surfaces. The fluid mass stored in the cracks is $M_{fc}^i = \rho_{fi}V_{ci}$, where the cracked volume can be expressed as $V_{ci} = \sum_{j=1}^3 A_{fj}^i \delta_{Nj}^i$, A_{fj}^i are the areas of six LDPM facets associated with the FLE A_{f1}^i, A_{f2}^i , and A_{f3}^i belonging to V_i ($i = 1, 2$), and δ_{Nj}^i are the normal crack openings, as shown in Fig. 2b and c.

The time variation of the fluid mass in the cracks can be written as:

$$\dot{M}_{fc}^i = \rho_{f0} \frac{V_{ci}}{K_f} \dot{p}_i + \rho_{fi} \dot{V}_{ci} \quad (13)$$

The fluid mass flux, Q_{fc} , from V_1 into V_2 associated with the cracks, can be approximated by assuming a steady laminar flow between two crack surfaces with a cross section of length l_{fj} and width δ_{Nj}^i with $j = 1, 2, 3$, where l_{fj} represents the intersection of the j th facet with

the tetrahedron face A (Fig. 2b). In this case, the solution of a two-dimensional Poiseuille flow in a channel, known as Poiseuille's formula, can be adopted [38]. One can write

$$Q_{fc} = \bar{\rho}_f \frac{\kappa_c}{\mu_f} A \frac{p_1 - p_2}{l} \quad (14)$$

where

$$\kappa_c = \frac{1}{12A} \left(\frac{g_2}{I_{c1}} + \frac{g_1}{I_{c2}} \right)^{-1} \quad (15)$$

and $I_{ci} = \sum_{j=1}^3 l_{fj} (\delta_{Nj}^i)^3$ ($i = 1, 2$). Connection in series of the cracked permeabilities in V_{c1} and V_{c2} is assumed for deriving Eq. 15.

Mass Balance Equations

The total fluid mass and total fluid flux can be obtained by adding the contributions from the uncracked and cracked domains. By collecting all terms introduced above and normalized both left and right hand sides with the reference fluid density ρ_{f0} , the mass balance equations for volume V_1 and V_2 can be written as:

$$\begin{aligned} \left(b\dot{e}_{v1} + \frac{\dot{p}_1}{M_b} \right) V_1 + \frac{V_{c1}\dot{p}_1}{K_f} + \frac{\rho_{f1}\dot{V}_{c1}}{\rho_{f0}} + Q_{fu} + Q_{fc} &= 0 \\ \left(b\dot{e}_{v2} + \frac{\dot{p}_2}{M_b} \right) V_2 + \frac{V_{c2}\dot{p}_2}{K_f} + \frac{\rho_{f2}\dot{V}_{c2}}{\rho_{f0}} - Q_{fu} - Q_{fc} &= 0 \end{aligned} \quad (16)$$

3.2 The Lattice Discrete Particle Model (LDPM) implementation

Following the discrete formulation of the FLE [58], by defining the discrete estimation of pore pressure flux in Eq. 12 as:

$$g_p = \mathbf{e} \cdot \mathbf{n} (p_2 - p_1) / l \quad (17)$$

where p_1, p_2 are the values of fluid pressure at points N_1 and N_2 , respectively, the governing equations for a FLE volume equivalent to Eqs. 16 can be rewritten as:

$$\begin{aligned} \left(b\dot{e}_{v1} + \frac{\dot{p}_1}{M_b} \right) V_1 + \frac{V_{c1}\dot{p}_1}{K_f} + \frac{\rho_{f1}\dot{V}_{c1}}{\rho_{f0}} + \xi \frac{A}{l} (p_2 - p_1) &= 0 \\ \left(b\dot{e}_{v2} + \frac{\dot{p}_2}{M_b} \right) V_2 + \frac{V_{c2}\dot{p}_2}{K_f} + \frac{\rho_{f2}\dot{V}_{c2}}{\rho_{f0}} - \xi \frac{A}{l} (p_2 - p_1) &= 0 \end{aligned} \quad (18)$$

where the effective permeability reads $\xi = \bar{\rho}_f (\kappa_0 + \kappa_c) / (\rho_{f0}\mu_f)$. The discrete-type governing equations in Eqs. 18 can then written in the matrix form, which reads:

$$\mathbf{M}\dot{\mathbf{p}} + \mathbf{K}\mathbf{p} + \mathbf{S} = \mathbf{0} \quad (19)$$

where,

$$\mathbf{M} = V \begin{bmatrix} g_1 C_1 & 0 \\ 0 & g_2 C_2 \end{bmatrix} \quad (20)$$

$$\mathbf{K} = \frac{A}{l} \begin{bmatrix} \xi & -\xi \\ -\xi & \xi \end{bmatrix} \quad (21)$$

$$\mathbf{S} = V \begin{bmatrix} g_1 S_1 & g_2 S_2 \end{bmatrix}^T \quad (22)$$

$$\mathbf{p} = \begin{bmatrix} p_1 & p_2 \end{bmatrix}^T \quad (23)$$

where $C_i = M_b^{-1} + V_{ci}(K_f V_i)^{-1}$ and $S_i = b e_{vi} + \rho_{fi} V_c (\rho_{f0} V_i)^{-1}$. It is worth observing that, to reduce the memory requirements of the calculations, it is possible, without significant difference in the results, to substitute C_i and $S_i (i = 1, 2)$ with the volume averages $\bar{C} = g_1 C_1 + g_2 C_2$ and $\bar{S} = g_1 S_1 + g_2 S_2$. The global matrices of the overall governing equations of the flow problem are obtained by assembling the matrix contributions of all flow elements. There are various types of boundary layer elements as introduced in [58], Dirichlet-type boundary conditions can be directly imposed on the external nodes of the boundary layers. The fluxes of the boundary layer elements can also be calculated. The volumetric flow rate over the boundaries can be estimated through the sum of the fluxes (Riemann sum), given the perpendicularity of the boundary layer elements to the model boundaries. In this work, the time integration of the flow problem was performed by means of the Backward Euler method.

Following [58], the M-LDPM implementation of poroflow in Abaqus should use the incremental form of the governing equations, which are given by:

$$\begin{aligned} \mathbf{f}(\mathbf{u}_{n+1}) &\approx \mathbf{f}(\mathbf{u}_n) + \frac{\partial \mathbf{f}(\mathbf{u}_n)}{\partial \mathbf{u}} \Delta \mathbf{u} = \mathbf{0} \\ \frac{\partial \mathbf{f}(\mathbf{u}_n)}{\partial \mathbf{u}} \Delta \mathbf{u} &= -\mathbf{f}(\mathbf{u}_n) \end{aligned} \quad (24)$$

where

$$\mathbf{f}(\mathbf{u}) = \begin{bmatrix} f_1 \\ f_2 \end{bmatrix} = \begin{bmatrix} Vg_1C_1\dot{p}_1 + A\xi/l(p_1 - p_2) + Vg_1S_1 \\ Vg_2C_2\dot{p}_2 - A\xi/l(p_1 - p_2) + Vg_2S_2 \end{bmatrix} \quad (25)$$

The element level entries of the Jacobian matrix and the right-hand side vector corresponding

to Eqs. 24 and 25 are calculated by:

$$\frac{\partial \mathbf{f}(\mathbf{u}_n)}{\partial \mathbf{u}} = \begin{bmatrix} \partial f_1 / \partial p_1 & \partial f_1 / \partial p_2 \\ \partial f_2 / \partial p_1 & \partial f_2 / \partial p_2 \end{bmatrix} \quad (26)$$

and

$$-\mathbf{f}(\mathbf{u}) = -\begin{bmatrix} f_1 & f_2 \end{bmatrix}^T \quad (27)$$

In contrast to continuous or other discrete models, in which the same nodal sites are often used to represent mechanical (i.e., displacements) and flow-related quantities (e.g., moisture content and temperature), in topologically dual systems of lattice models, the nodal sites of the transport/flow network and mechanical lattices are always different. Furthermore, a challenge arises if different solvers are chosen for different analyses (e.g., explicit for mechanical solver, implicit for flow solver), as the time step sizes would then vary substantially. Different meshes and time scales of the coupled fields can complicate the coupling process (also referred to as “multidomain” or “multimodel” coupling). In the following section, a framework for coupled analyses of lattice models will be discussed.

4 Two-way coupling framework

The multiphysics problems, with the example of the fully two-way coupled poroflow problem, can be solved in the so-called M-LDPM framework with the help of Interprocess Communication (IPC). Under this framework, each physical solver can be considered as an independent process. The periodic data communication between processes (e.g., Abaqus/standard solver for the flow part and Abaqus/Explicit solver for the mechanical part) allows a sequential

coupling mechanism. The spatial mappings and temporal synchronization between the two processes allow the coupling to run smoothly and robustly.

4.1 Coupling Procedure

In the two-way coupling procedure, the algorithms are implemented through Abaqus user-defined elements *VUEL* for the LDPM and *UEL* for the FLM . Abaqus solvers (Abaqus/standard for the FLM and Abaqus/Explicit for the LDPM) control the flow events in the respective analysis and the data exchange between both models is achieved via the IPC. The main steps that achieve the two-way communication during a single integration time step are introduced below following a temporal ordering, for LDPM: (1) update the element dynamics (nodal positions, geometries), (2) exchange data with the coupled analysis (i.e. FLM), (3) compute strains, and stresses based on the constitutive models and multiphysics coupling mechanisms, (4) compute internal forces on the LDPM elements; For FLM, the steps are (1) update the element field variables (nodal pore pressures), (2) exchange data with the coupled analysis (i.e. LDPM), (3) compute the tangential stiffness matrix (jacobian or AMATRX matrix) and the right-hand side vector (RHS vector), (4) iteratively compute increment until the convergence is reached.

In the M-LDPM framework, the data that needs to be exchanged between solvers are mainly the field variables. For example, during the coupled analysis, the crack openings on LDPM facets need to be passed from LDPM side to FLM side, in order to calculate the crack-enhanced permeability/conductivity. Aparts from the field variables, model settings or parameters of the two models can be passed to each other for initialization purposes.

Each tet element in LDPM mesh is corresponding to a tet point (node) in FLM mesh, the tet point nodal value will be mapped to 12 facets in the corresponding tet element. In such a way, each tet element has a uniform value in the diffusion field, because all 12 facets have

the same value to the corresponding tet point.

It is worth noting that all the simulations in this work were done on a single processor within a single thread. There is a huge potential to speed up the simulations by parallelizing the mechanical and flow problems over several processors. Parallelization of LDPM simulations is relatively straightforward, as the explicit time integration scheme is naturally suitable for the domain-level (split the model into a number of topological domains) or loop-level (parallelizes element operation loops in the code) parallelization. On the contrary, the parallelization of the FLM simulations is less effective, as the flow problems typically favor the implicit schemes (to achieve relatively large time steps), which require direct solving of large sparse matrices. The parallelization can be either made in element operations for the matrix solving or can be made through sophisticated matrix solving techniques. However, this is beyond the scope of this work and will remain as a subsequent topic.

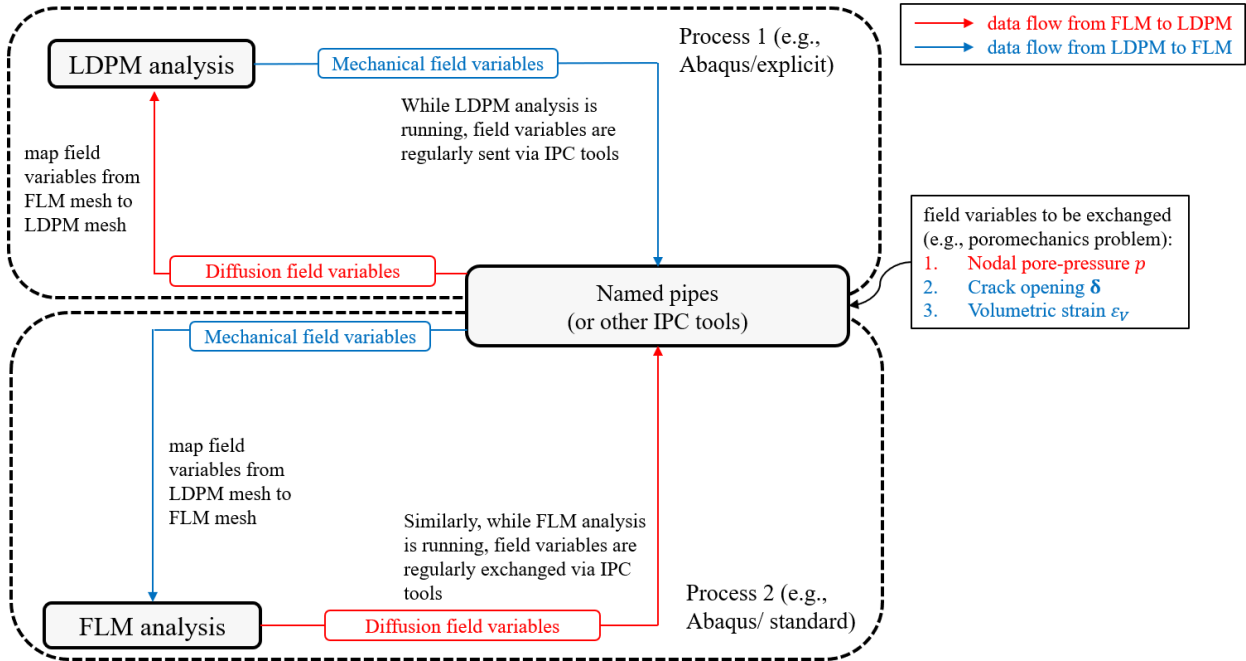


Figure 3: schematic diagram of M-LDPM two-way coupling procedure

4.2 Data communication between solvers

Inter-process communication (IPC) refers to the coordination of activities among cooperating processes. This communication could involve a process letting another process know that some event has occurred or the transferring of data from one process to another. For our applications of IPC in solving Multiphysics problems, the processes are numerical ODE/PDE solvers (e.g., Abaqus/Ansys/in-house codes/other solvers). Typical IPC media include shared memory, sockets, and pipes [33, 34]. Among these, named pipes are employed as the IPC media in this work.

Named pipes are a simple synchronized way of passing information between two processes. A named pipe can be viewed as a special file that can store data and uses a “First In First Out (FIFO)” access scheme to retrieve data. A named pipe can exist independently of the process. In a logical view of a pipe, data is written to one end and read from the other, as shown in Fig. 4. The system provides synchronization between the reading and writing process. It also solves the producer/consumer problem: writing to a full pipe automatically blocks, as does reading from an empty pipe. The system also assures that there are processes on both ends of the pipe at all time. The programmer is still responsible, however, for preventing deadlock between processes [34].

During a two-way coupling analysis, each process suspends operations periodically at one of two locations, referred to as synchronization points, and performs a data exchange with the coupled process, as illustrated in Fig. 4. The first synchronization point is located at the initialization step of the analysis, prior to commencing the first time increment. This synchronization point will be called only once and, hence, allows for initial configurations to be exchanged between processes. The second synchronization point occurs at the end of a completed increment when the target time is reached in each process. This synchronization point is called multiple times as the simulation advances in time. At every synchronization

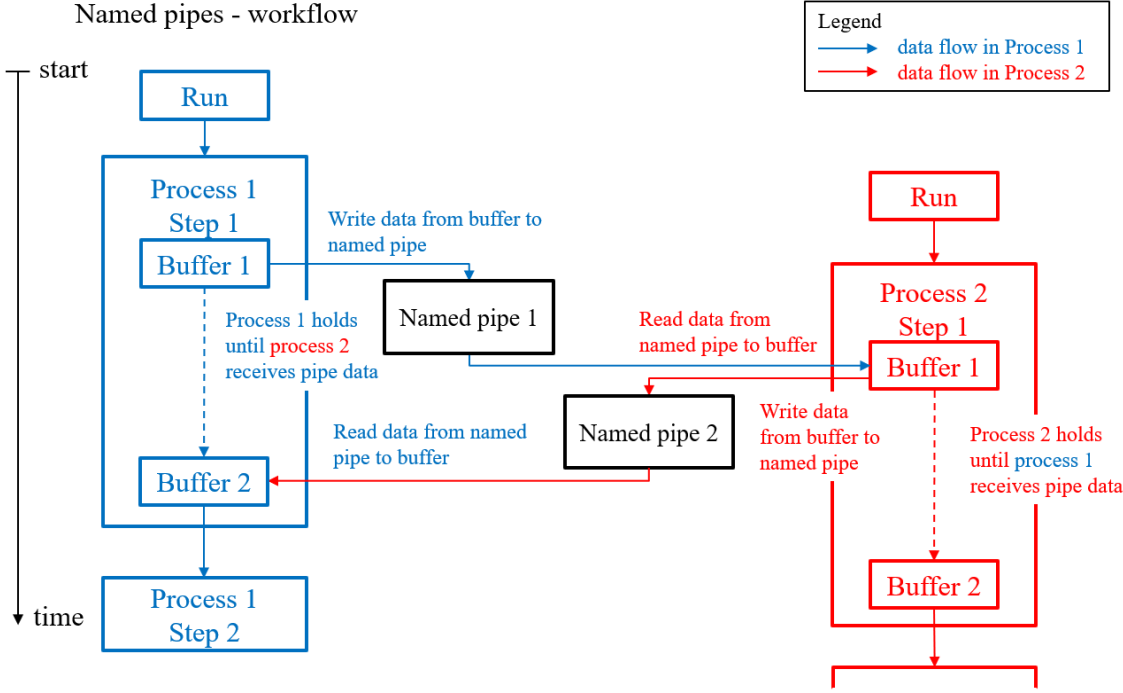


Figure 4: Schematic diagram of the Inter-process Communication (IPC) between solvers at a synchronization point

point each process waits to receive the requested data from the coupled process before continuing. Therefore, for a two-way coupled simulation the synchronization point represents a point when both analyses coincide in solution time.

4.3 Coupling and time incrementation schemes

4.3.1 Coupling scheme

There are two typical coupling schemes: (1) parallel explicit coupling scheme (a.k.a. Jacobi scheme), both simulations are executed concurrently, exchanging fields to update the respective solutions at the next target time. This scheme is more efficient in the use of computing resources; less stable than the sequential scheme; (2) sequential explicit coupling scheme (a.k.a. Gauss-Seidel scheme), the simulations are executed in sequential order. One analysis leads while the other analysis lags the simulations. The parallel explicit coupling

(Jacobi) scheme is used in this work. Figure 5 illustrates the parallel coupling scheme, the horizontal lines represent simulation time. The dots represent increments (or time steps) for a particular analysis in the coupled simulation. The dashed vertical arrows denote data exchange in the direction of the arrowheads between the analysis codes.

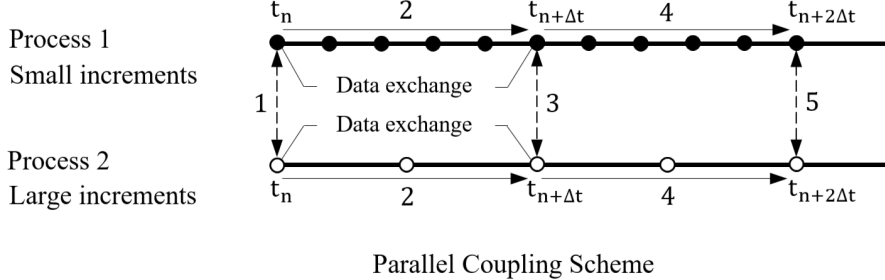


Figure 5: Parallel explicit coupling (Jacobi) scheme for the data exchange, modified from [30].

4.3.2 Time incrementation scheme

In many applications, the coupled two processes may have very distinct scales of time increments (e.g., for a coupled poroflow problem, explicit mechanical analysis has a stable time increment typically ranged 10^{-7} – 10^{-3} s, while implicit flow analysis has no stable time increment requirement, but for better convergence a time increment ranged 10^{-1} – 10^3 s is used).

When the time increments of coupled two processes differ largely, one may use time scaling factor, k_{time} , to scale the time increment of one analysis for the synchronization, or use other techniques such as subcycling time incrementation scheme (see Fig. 6). In subcycling, the analysis with a larger time increment (generally, the implicit analysis) ramps loads from the values of the previous coupling step to the values at the target time. In the analysis with a smaller time increment (generally, the explicit analysis) the loads are applied at the start of the coupling step and kept constant over the coupling step. Given the large discrepancy in the time increments of two coupled analyses, and to save the computational cost, both the

time scaling factor and subcycling approach are used in this work.

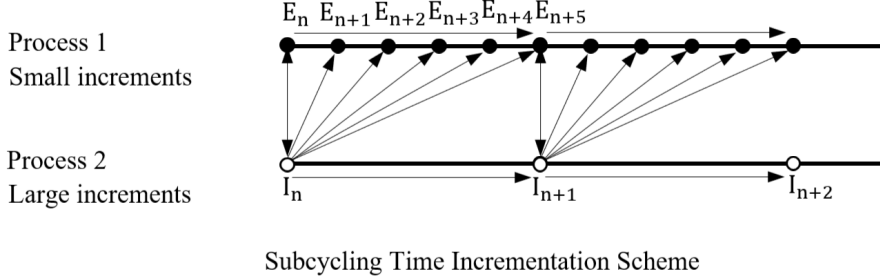


Figure 6: Subcycling time incrementation scheme, modified from [30]. For M-LDPM, Code A or “E” stands for explicit mechanical analysis; Code B or “I” stands for implicit flow analysis.

5 Numerical example

The two-way coupling framework is verified by three examples: (i) Terzaghi’s consolidation, (ii) radial expansion of pressurized hollow cylinder, and (iii) hydraulic fracturing of hollow cylinder. These verification exercises are essential to ensure that the numerical model accurately represents and correlates to the governing equations intended to be solved and hence establish credibility for the modeling effort. All verification examples involve only simple geometries and boundary conditions but are representative of verifying at least one aspect of the model implementation of the coupling mechanisms. Reference (mostly theoretical) solutions are attached to the current simulation outcomes.

We note that the mesoscale discrete model exhibits intrinsic randomness due to the randomized generation rules of material’s mesostructure. Hence, the generation of the material’s mesostructure is repeated three times with the same parameters and the average results of three generations for all the examples are used.

5.1 Benchmark 1: Terzaghi's 1D consolidation

The first numerical example is the classical one-dimension consolidation problem of Terzaghi [52], in light of the Biot's theory. A $0.5 \times 0.1 \times 0.1 \text{ m}^3$ prism equivalent to infinite soil layer of thickness $L = 0.5 \text{ m}$ on a rigid impervious ground, is loaded by a stress $\sigma_z = t_z^*$ on the top surface at $z = 0$ under drained condition, the Dirichlet boundary conditions are $p = 0$ at $z = 0$ for the pore pressure, and $u_z = 0$ at $z = L$, $u_x = u_y = 0$ at all lateral surfaces for the displacement. According to [16], this loading case is also called mode 1. A schematic diagram of the numerical example is shown in Fig. 7a. LDPM and FLM meshes generated are shown in Fig. 8.

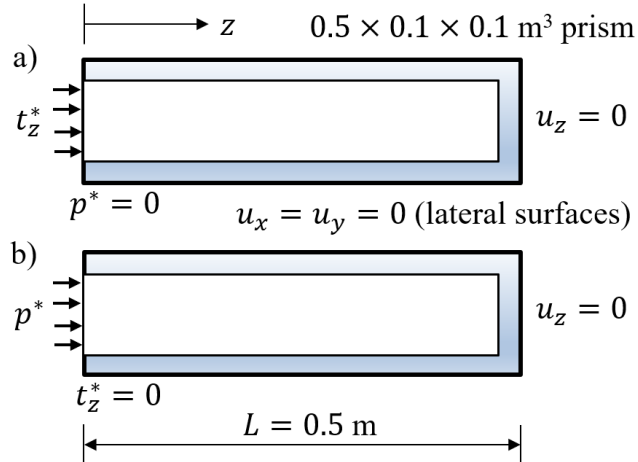


Figure 7: Two-way coupling verification 1: Terzaghi's 1D consolidation, simulation settings: a) loading by pressure, b) loading by traction.

In the absence of body force, σ_z is independent of z . The differential equation for u_z (the Navier equation) reads:

$$\frac{2G(1-\nu)}{1-2\nu} \frac{\partial^2 u_z}{\partial z^2} - b \frac{\partial p}{\partial z} = 0 \quad (28)$$

where $G = E_c/(2+2\nu)$ is the macroscopic shear modulus of the drained soil, $E_c = E_0(2+3\alpha)/(4+\alpha)$ is the macroscopic drained elastic modulus, $\nu = (1-\alpha)/(4+\alpha)$ is the macroscopic drained Poisson's ratio, E_0 is the mesoscopic normal modulus, α is the mesoscopic normal-

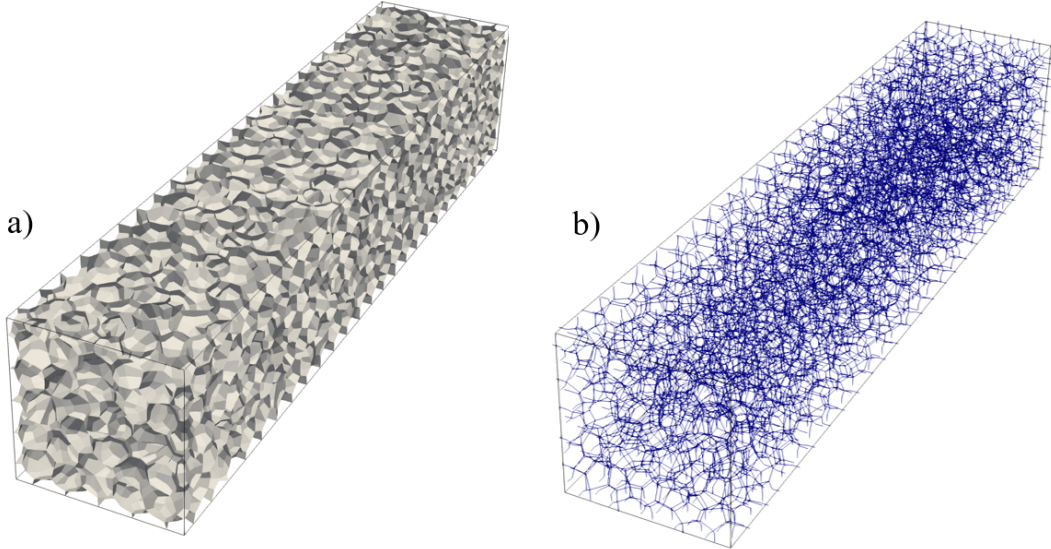


Figure 8: The LDPM tessellation of the prism's geometry for Terzaghi's 1D consolidation: a) LDPM mesh, b) FLM mesh.

to-shear coefficient, b is the Biot coefficient. According to Biot's theory for the uniaxial strain problems, the diffusion equation for the pore pressure is:

$$\frac{\partial p}{\partial t} - c \frac{\partial^2 p}{\partial z^2} = -\frac{\Upsilon}{GS} \frac{d\sigma_z}{dt} \quad (29)$$

where c is the diffusivity coefficient $c = \kappa/S = [2\kappa G(1-\nu)(\nu_u - \nu)]/[b^2(1-2\nu)^2(1-\nu_u)]$, κ is the intrinsic permeability of the soil, c is also called generalized consolidation coefficient or Terzaghi consolidation coefficient under 1D consolidation; $\Upsilon = b(1-2\nu)/(2-2\nu)$, S represents a storage coefficient, $S = (1-\nu_u)(1-2\nu)/[M(1-\nu)(1-2\nu_u)]$, M is the Biot modulus, ν_u is the undrained Poisson's ratio, $\nu_u = (3K_u - 2G)/[2(3K_u + G)]$, K_u stand for the undrained bulk modulus and reads $K_u = M_b b^2 + E_c/[3(1-2\nu)]$, M_b is the Biot modulus. The values of parameters used in this section are summarized in Tab. 1.

Since the stress on the boundary is a constant, the right hand side of Eq. (29) drops out to

give a homogeneous diffusion equation:

$$\frac{\partial p}{\partial t} - c \frac{\partial^2 p}{\partial z^2} = 0 \quad (30)$$

The two fields $p^{(1)}$ and $u_z^{(1)}$ can be expressed in terms of the dimensionless coordinate $\chi = z/L$ and the dimensionless time $\tau = ct/(4L^2)$, where t is the real time. Solving Eq. (30) with the above initial and boundary conditions yields:

$$p^{(1)} = \frac{\Upsilon t_z^*}{GS} [1 - F_1(\chi, \tau)] \quad (31)$$

where

$$F_1(\chi, \tau) = 1 - \sum_{m=1,3,\dots}^{\infty} \frac{4}{m\pi} \sin\left(\frac{m\pi\chi}{2}\right) \exp(-m^2\pi^2\tau) \quad (32)$$

The displacement $u_z^{(1)}$ can be similarly expressed in terms of the dimensionless coordinate χ and the dimensionless time τ as:

$$u_z^{(1)} = \frac{t_z^* L (1 - 2\nu_u)}{2G (1 - \nu_u)} (1 - \chi) + \frac{p^* L (\nu_u - \nu)}{2G(1 - \nu) (1 - \nu_u)} F_2(\chi, \tau) \quad (33)$$

where

$$F_2(\chi, \tau) = \sum_{m=1,3,\dots}^{\infty} \frac{8}{m^2\pi^2} \cos\left(\frac{m\pi\chi}{2}\right) [1 - \exp(-m^2\pi^2\tau)] \quad (34)$$

Another loading case (mode 2) is that the surface at $z = 0$ is subjected to a fluid pressure p^* , as shown in Fig. 7b. In this case, only the boundary conditions at $z = 0$ are different: $\sigma_z = 0$ and $p = p^*$. The initial pore pressure field for mode 2 loading is everywhere zero.

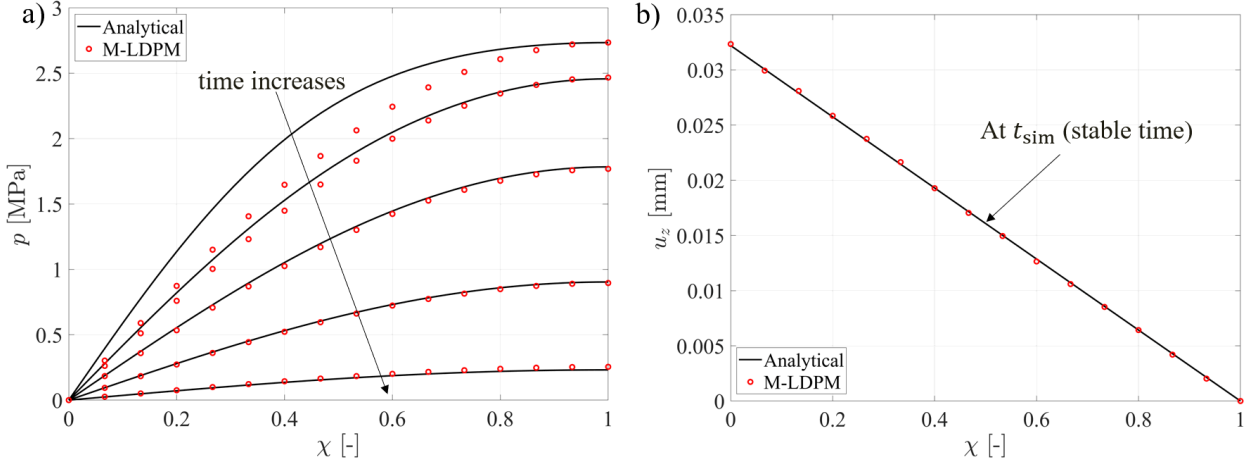


Figure 9: Terzhagi's consolidation, loading by traction: a) fluid pressure versus dimensionless coordinate $\chi = z/L$ at various times of simulation $t = 1/16t_{\text{sim}}, 1/8t_{\text{sim}}, 1/4t_{\text{sim}}, 1/2t_{\text{sim}}, t_{\text{sim}}$, and b) z displacement profiles versus dimensionless coordinate $\chi = z/L$ at t_{sim} .

The solution of $p^{(2)}$ is thus given by:

$$p^{(2)} = p^* F_1(\chi, \tau) \quad (35)$$

The pore pressure in the layer increases with time until it reaches the constant value p^* at $\tau = \infty$. The displacement field is again found by integrating (28):

$$u_z^{(2)} = -\frac{\Upsilon p^* L}{G} F_2(\chi, \tau) \quad (36)$$

We observe that the surface displacement is zero at $\tau = 0$, and gradually rebounds (instead of consolidating) to the long-term value of $u_z^{(2)} = -\Upsilon p^* L/G$. The rebound is a consequence of the dilation of the porous solid induced by an increase of the pore pressure.

At the instant of loading, the layer immediately consolidates to $u^* = p^* L(1 - 2\nu_u)/[2G(1 - \nu_u)]$. Two opposing processes then follows: one consolidates to the maximum value $p^* L(\nu_u - \nu)/[2G(1 - \nu)(1 - \nu_u)]$, and the other rebounds to the asymptotic value of $-\Upsilon p^* L/G$.

The solution of this problem is then obtained by superposition of the solutions of the two

modes. For example, the surface displacement is given by the sum of (33) and (36). It can be shown that the second process is always greater in magnitude than the first, but that it is never able to overcome the initial settlement. Hence the layer ends up with a positive settlement which is smaller than the initial one.

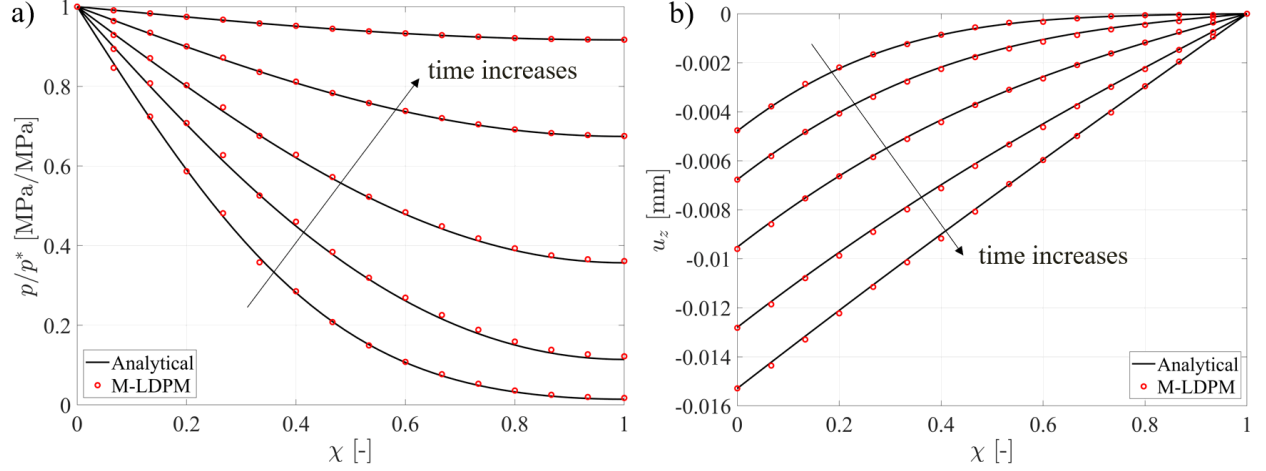


Figure 10: Terzaghi's consolidation, loading by fluid pressure: a) dimensionless fluid pressure p/p^* versus dimensionless coordinate $\chi = z/L$, and b) z displacement profiles u_z versus dimensionless coordinate $\chi = z/L$ at various times of simulation $t = 1/16t_{\text{sim}}, 1/8t_{\text{sim}}, 1/4t_{\text{sim}}, 1/2t_{\text{sim}}, t_{\text{sim}}$.

The two-way coupling simulation results of loading mode 1 and 2 are presented in Figs. 9 and 10, respectively. Dimensionless fluid pressure p/p^* , as well as z displacement profiles u_z versus dimensionless coordinate $\chi = z/L$ at different time instants $t = 1/16t_{\text{sim}}, 1/8t_{\text{sim}}, 1/4t_{\text{sim}}, 1/2t_{\text{sim}}, t_{\text{sim}}$. It turned out that numerical model results agree well with the analytical solution, showing the validity of the two-way coupling framework on the simulation of poroelasticity problems.

Table 1: Input parameters for two-way coupling simulations of poroelasticity (1D Terzaghi's consolidation)

Description	Symbol [unit]	Value
Density of fluid	ρ_f [kg/m ³]	1.0E+03
Dynamic viscosity of fluid	μ_f [Pa.s]	8.9E-04
Bulk modulus of fluid	K_f [Pa]	2.15E+09
Intrinsic permeability	κ_0 [m ²]	1.97E-20
Biot modulus	M_b [Pa]	6.1728E+10
Biot coefficient	b [-]	0.5
Reference pressure	p_0 [Pa]	0.0
Density of solid	ρ_s [kg/m ³]	2.46E+03
Mesoscopic normal modulus of solid	E_0 [Pa]	2.15E+10
Mesoscopic normal-to-shear coefficient of solid	α [-]	0.3
Time scaling factor	k_{time} [-]	17.28E+06
Total simulation time	t_{sim} [s]	5E-02

5.2 Benchmark 2: Radial expansion of a pressurized hollow cylinder

The injection of fluid into porous media is a problem of great interest in environmental engineering, biomechanics, and petroleum engineering. This interest has led to the development of analytical solutions for several idealized situations. One of the most commonly used analytical solutions in this class is derived for the pressurized hollow cylinder problem in the plane strain setting [27, 43, 45]. Consider a homogeneous elastic half-space (idealized as a thick hollow cylinder) subjected to a sudden continuous mass influx of pore fluid. The geometry of the hollow cylinder can be described by a $r - \theta - z$ cylindrical coordinate system with the inner surface at $r = r_i = 0.1$ m, the outer surface at $r = r_o = 0.725$ m, and the thickness $d = 0.1$ m, as shown in Fig. 11. The generated LDPM and FLM meshes are shown in Fig. 12. The values of parameters used in this section are summarized in Tab. 2. The constant influx of pore fluid has the magnitude of $p_{fi} = 50$ MPa. The porous elastic solid near the fluid source (inner surface $r = r_i$) will first deform in an undrained manner, given that the fluid infiltration is too rapid to diffuse the pore fluid pressure. Over time, the

diffusion of pore fluid leads to deformation further in the radial direction. Eventually, given sufficient time, the poroelastic responses will transit from the undrained limit to the drained limit where there is no alternation in pore pressure at the steady-state.

We first consider the pure diffusion of pore fluid pressure in the hollow cylinder. The initial condition is a water-saturated material with mechanically free boundaries, zero fluid pressure at the outer boundary $r = r_o$, and a continuous fluid injection p_{fi} into the borehole $r = r_i$. The analytical solution of the radial fluid pressure distribution at steady-state reads [27]:

$$p_f = p_{fi} \frac{\log \frac{r_o}{r}}{\log \frac{r_o}{r_i}} \quad (37)$$

A typical example of results at steady-state is shown in Fig. 13. The final pressure profile fits almost precisely the analytical solution.

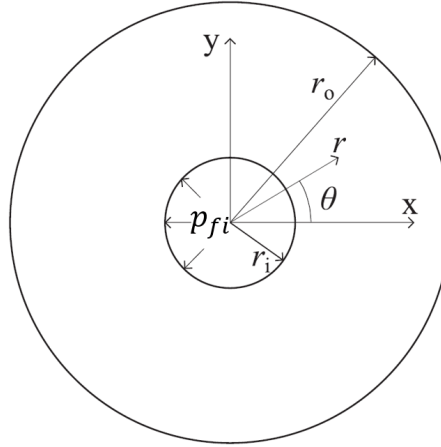


Figure 11: Two-way coupling verification 2: radial expansion of a pressurized hollow cylinder, simulation settings adopted from [27].

Apart from the flow analysis, we then move to the mechanical part of the pressurized hollow cylinder problem. Poroelastic radial expansion in the hollow cylinder due to the fluid

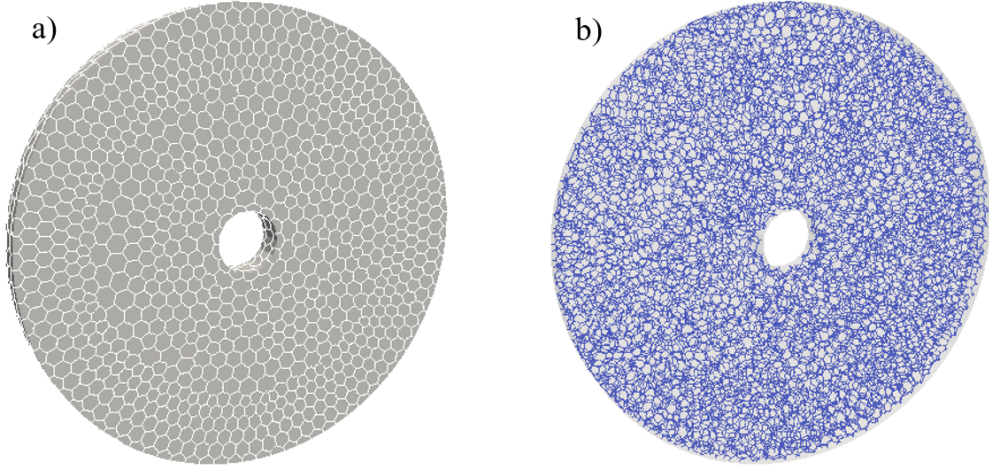


Figure 12: The LDPM tessellation of the hollow cylinder's geometry for the poroelastic radial expansion: a) LDPM mesh, b) FLM mesh.

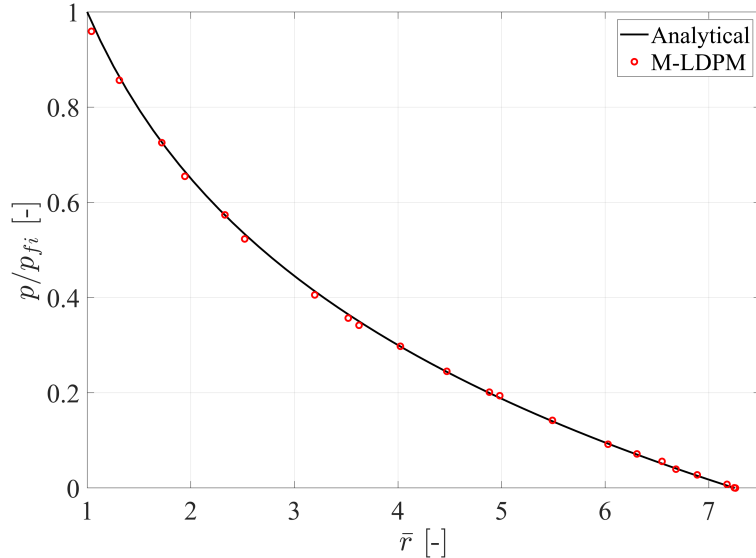


Figure 13: Radial fluid pressure distribution in a pressurized hollow cylinder at steady-state

injection, can be analytically resolved, the dimensionless radial displacement is given by [27]:

$$\bar{u} = -b\bar{p}_{fi} \frac{1-\nu^2}{2} \left[\frac{\bar{r}_o^2}{\bar{r}_o^2 - 1} \left(\frac{1+\nu}{1-\nu} \frac{1}{\bar{r}} + r \right) + r \frac{\frac{1}{1+\nu} - \ln \bar{r}}{\ln \bar{r}_o} \right] - (1-b)\bar{p}_{fi} \frac{\bar{r}_o^2}{\bar{r}_o^2 - 1} \left(\frac{1+\nu}{r} + \frac{\bar{r}(1-\nu)}{\bar{r}_o^2} \right) \quad (38)$$

where $\bar{u} = u/r_i$, $\bar{r} = r/r_i$, $\bar{r}_o = r_o/r_i$, $\bar{p}_f = p_f/E_c$, $\bar{p}_{fi} = p_{fi}/E_c$, $E_c = (2+3\alpha)/(4+\alpha)E_0$, $\nu = (1-\alpha)/(4+\alpha)$. It should be noted that since we want to model the poroelastic behavior of the cylinder only caused by the fluid pressure, the presence of boundary flow in this

Table 2: Input parameters for two-way coupling simulations of poroelasticity (radial expansion of a pressurized hollow cylinder)

Description	Symbol [unit]	Value
Density of fluid	ρ_f [kg/m ³]	1.0E+03
Dynamic viscosity of fluid	μ_f [Pa.s]	8.9E-04
Bulk modulus of fluid	K_f [Pa]	2.15E+09
Intrinsic permeability	κ_0 [m ²]	1.97E-20
Biot modulus	M_b [Pa]	6.1728E+10
Biot coefficient	b [-]	0/0.5/1.0
Reference pressure	p_0 [Pa]	0.0
Density of solid	ρ_s [kg/m ³]	2.46E+03
Mesoscopic normal modulus of solid	E_0 [Pa]	4.648E+10
Mesoscopic normal-to-shear coefficient of solid	α [-]	1.0/0.5455/0.1667 ¹
Time scaling factor	k_{time} [-]	9.0E+06
Total simulation time	t_{sim} [s]	5E-02

fluid injection problem, should be modeled with both the Dirichlet boundary condition of pore pressure p_{fi} and mechanical traction boundary condition σ_r . The total stress at the boundary should be equal to the fluid pore pressure, therefore, the mechanical (effective) stress at the boundary is zero. The constant influx of pore pressure $p_{fi} = 50$ MPa is applied at the surface r_i , and mechanical pressure with the same magnitude is applied to a very thin layer of elastic skin (modeled with S3R shell elements in Abaqus) at r_i . This elastic skin layer is tied with the LDPM boundary nodes and has the elastic modulus E_c and Poisson's ratio ν . Skin layer thickness is selected as 0.0025 m after a sensitivity analysis.

The results of injection simulations for various macroscopic Poisson's ratios $\nu = 0, 0.1, 0.2$ are shown in Fig. 14, Fig. 15, and Fig. 16, respectively. One may notice that the results generally fit the analytical solution well for $b = 0$ and $b = 0.5$. For $b = 1.0$, since the mechanical boundary conditions in the simulations and in the analytical solution are not identical, there is a displacement deviation far from the injection point, where a free boundary leads to a larger displacement and a fixed boundary naturally leads to a displacement that goes to zero at the domain perimeter. Moreover, it is obvious that there is a comparatively large discrepancy in the simulation and analytical results for larger Poisson's ratios, this is possibly

due to the intrinsic inconsistency in modeling the Poisson's effects with discrete/lattice models [6].

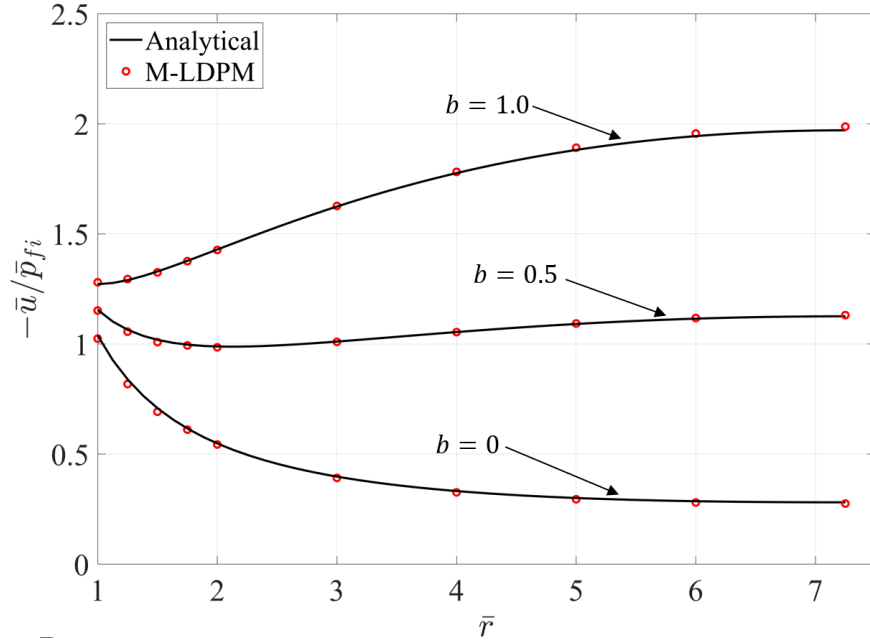


Figure 14: Radial expansion of a pressurized hollow cylinder, dimensionless radial displacement distribution $-\bar{u}/\bar{p}_{fi}$ versus dimensionless radial coordinate \bar{r} for Biot coefficient $b = 0, 0.5, 1$ and macroscopic Poisson's ratio $\nu = 0$

5.3 Benchmark 3: Hydraulic fracturing of hollow cylinder

In this section, we study the potential fracture formation caused by continuous fluid injection into the hollow cylinder that was studied in the previous section. The geometry and boundary conditions are the same as presented in Fig. 11. The values of parameters used in this section are summarized in Tab. 3, note that we present results for low-permeability rocks with $\kappa_0 = 1.97E-20 \text{ m}^2$. For all fracture analyses, $\nu = 0.1$ was assumed. Fracture formation is expected to affect the pore pressure diffusion process in the unfractured condition. Firstly, crack openings obviously allow increased mechanical displacement. This can cause increased expansion of the pressurized cylinder, which leads to a global pressure drop, and causes the formation of open volumes available for inflow of fluid in the bulk material. Secondly, crack

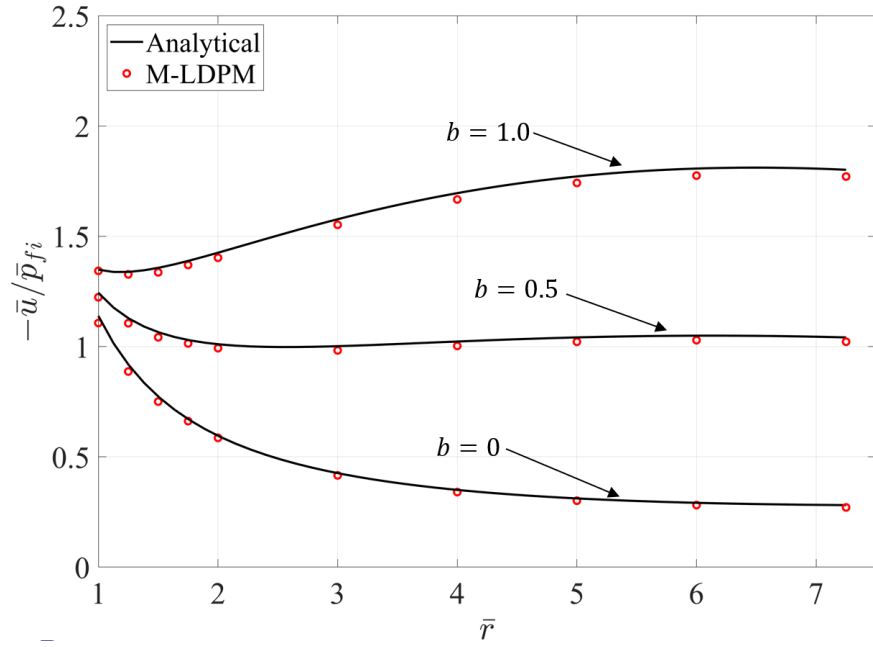


Figure 15: Radial expansion of a pressurized hollow cylinder, dimensionless radial displacement distribution \bar{u}/\bar{p}_{fi} versus dimensionless radial coordinate \bar{r} for Biot coefficient $b = 0, 0.5, 1$ and macroscopic Poisson's ratio $\nu = 0.1$

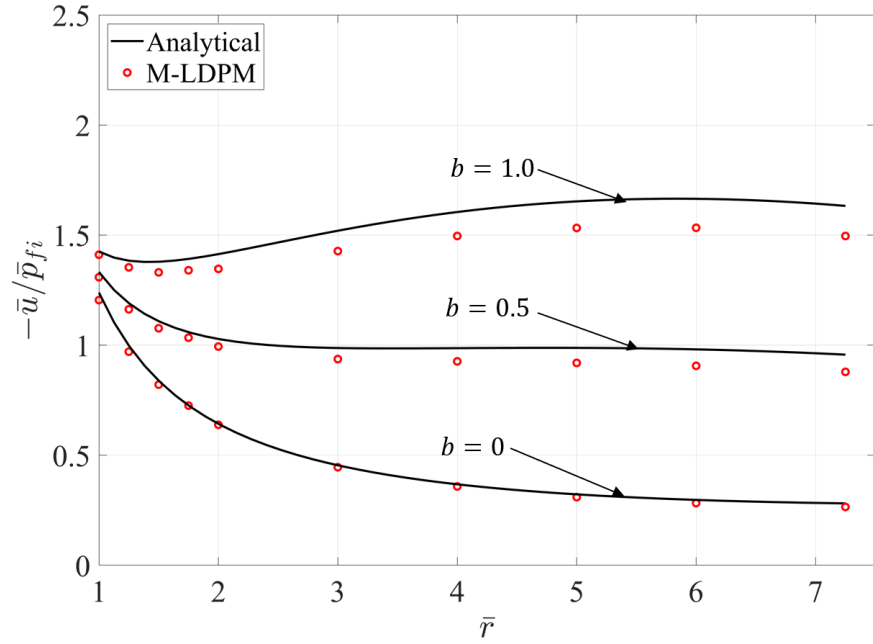


Figure 16: Radial expansion of a pressurized hollow cylinder, dimensionless radial displacement distribution \bar{u}/\bar{p}_{fi} versus dimensionless radial coordinate \bar{r} for Biot coefficient $b = 0, 0.5, 1$ and macroscopic Poisson's ratio $\nu = 0.2$

Table 3: Input **relevant** parameters for two-way coupling simulations of hydraulic fracturing of a pressurized hollow cylinder

Description	Symbol [unit]	Value
Density of fluid	ρ_f [kg/m ³]	1.0E+03
Dynamic viscosity of fluid	μ_f [Pa.s]	8.9E-04
Bulk modulus of fluid	K_f [Pa]	2.15E+09
Intrinsic permeability	κ_0 [m ²]	1.97E-20
Biot modulus	M_b [Pa]	6.1728E+10
Biot coefficient	b [-]	0/0.5/1.0
Reference pressure	p_0 [Pa]	0.0
Density of solid	ρ_s [kg/m ³]	2.46E+03
Mesoscopic normal modulus of solid	E_0 [Pa]	4.648E+10
Mesoscopic normal-to-shear coefficient of solid	α [-]	0.5455
Mesoscopic tensile strength of solid	σ_t [Pa]	4.648E+06
Mesoscopic tensile characteristic length of solid	l_t [m]	0.2
Mesoscopic normal-to-shear strength ratio of solid	r_{st} [-]	4.1
Mesoscopic softening exponent of solid	n_t [-]	0.2
Mesoscopic compressive yielding stress of solid	σ_{c0} [Pa]	1E+08
Mesoscopic initial internal friction coefficient of solid	μ_0 [-]	0.2
Mesoscopic asymptotic internal friction coefficient of solid	μ_∞ [-]	0.0
Mesoscopic transitional normal stress of solid	σ_{N0} [Pa]	6E+08
Mesoscopic softening exponent of solid	H_0 [-]	0.2
Time scaling factor	k_{time} [-]	9.0E+06
Total simulation time	t_{sim} [s]	5E-02

openings will increase the permeability of the corresponding flow volume and thus lead to more efficient drainage of the injected fluid.

The simulation results until the divergence of the solver due to the fracturing are presented in Fig. 17 in the form of normalized pressure \bar{p}_{fi} versus normalized radial displacement \bar{u} at the inner boundary for $b = 0, 0.5$ and 1 . Noticing that for the simulations with $b = 0$, we completely disabled the coupling procedure: the corresponding results in this section represent the uncoupled condition, no volumetric and cracking effects were involved. It can be observed that, Biot's coefficient has a strong influence on pressure–displacement curves in Fig. 17. This can be interpreted as: with the coupling, the crack-induced augmentation in permeability helps the faster drainage of pore pressure, and it reciprocally assists the

further and crack growth in material, leading to the overall decrease in the peak load of the material. Stronger the coupling (higher the Biot coefficient), lower the peak load the material can resist.

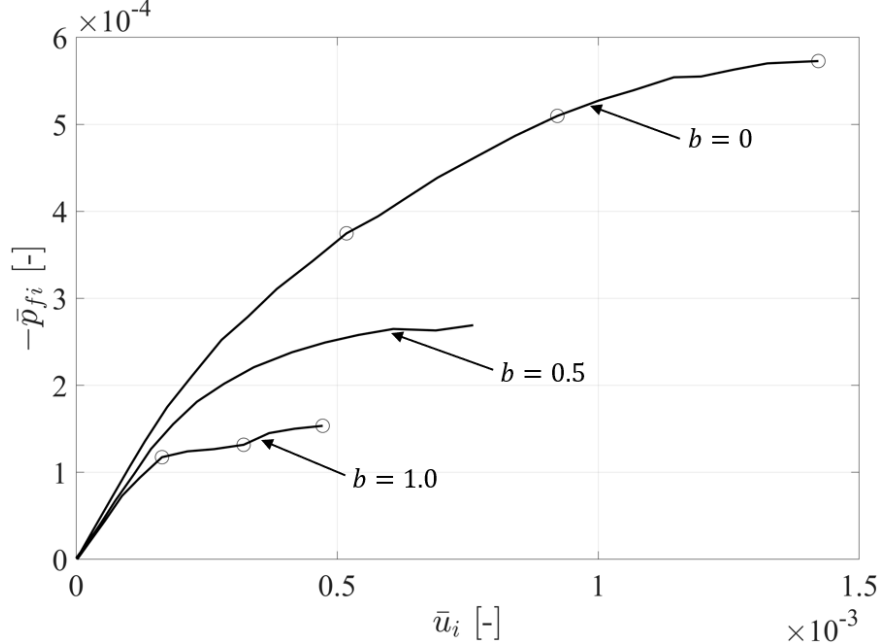


Figure 17: M-LDPM simulations of hydraulic fracturing of a pressurized hollow cylinder, normalized pressure \bar{p}_{fi} versus normalized radial displacement \bar{u} at the inner boundary at $r = r_i$. The circles indicate moments at which the crack patterns are shown in Figs. 18 and 19 for $b = 0$ and 1, respectively

The circles in Fig. 17 indicate the moments at which the crack patterns are presented in Figs. 18 and 19 for $b = 0$ and $b = 1$, respectively. From Figs. 18 and 19, the crack patterns change with Biot coefficient obviously: there is more diffused microcracking appearing at the critical pressure around the central hole for low Biot coefficients. This is due to different pressure magnitudes sustained by models with different Biot coefficients. If one studies the cracking at the same pressure level, the situation is actually the opposite: the larger Biot coefficients give more diffused cracking because the fluid pressure reduces both radial and circumferential compressive stresses in the solid. Since it further helps to open the cracks, the critical pressure for larger Biot coefficients is substantially lower.

The pore pressure contours corresponding to crack patterns in Figs. 18 and 19 for $b = 0$

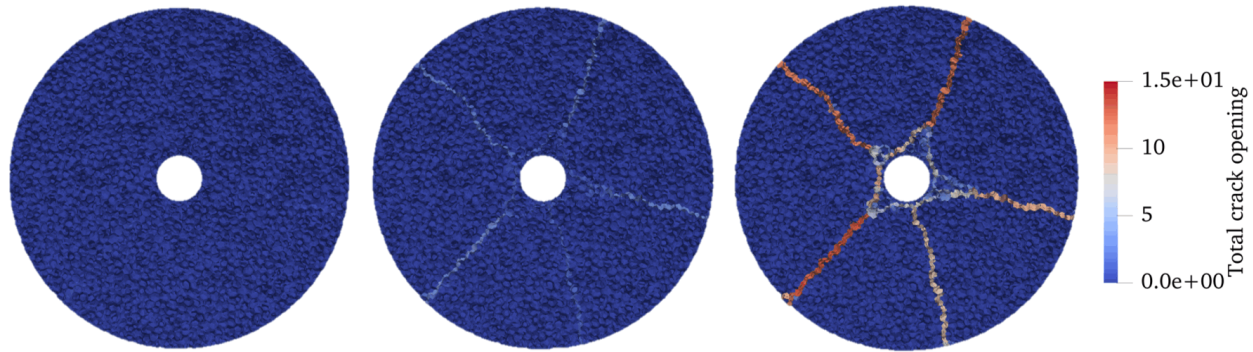


Figure 18: Crack patterns (crack opening contours) for uncoupled condition ($b = 0$) at three moments shown in Fig. 17.

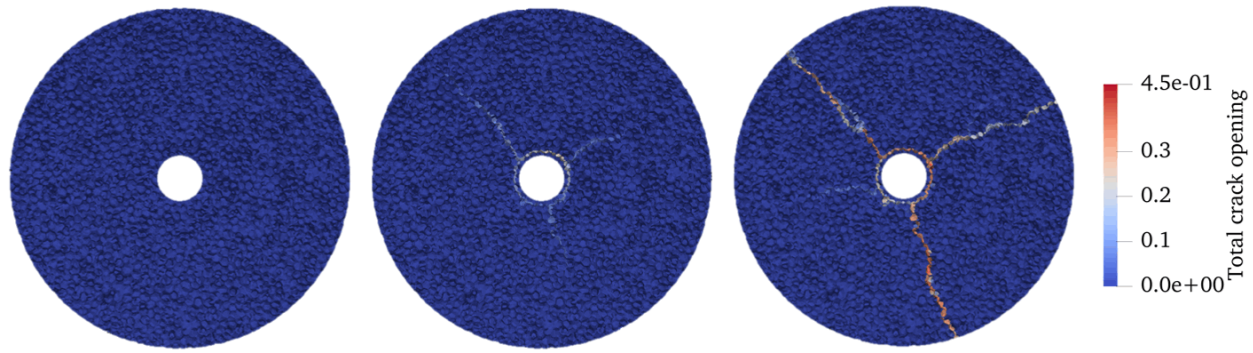


Figure 19: Crack patterns (crack opening contours) for $b = 1.0$ at three moments shown in Fig. 17.

and $b = 1$ are shown in Figs. 20 and 21, respectively.

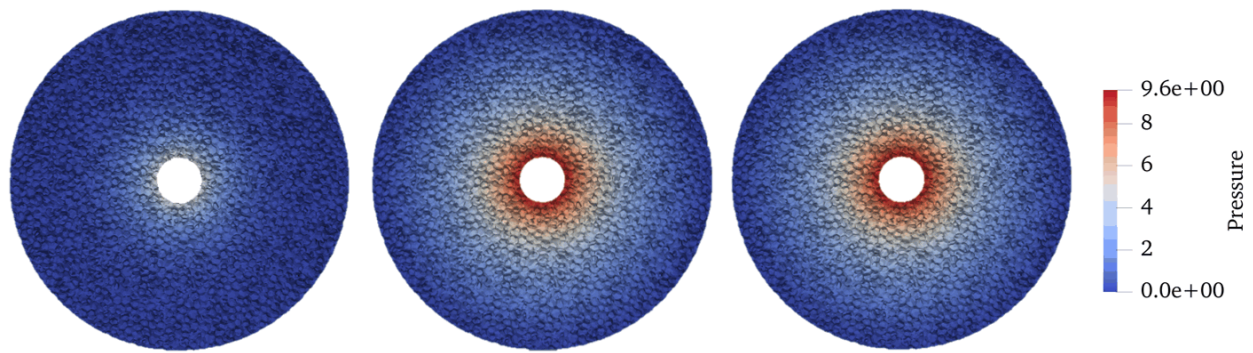


Figure 20: Pore pressure contours for uncoupled condition ($b = 0$) at three moments shown in Fig. 17.

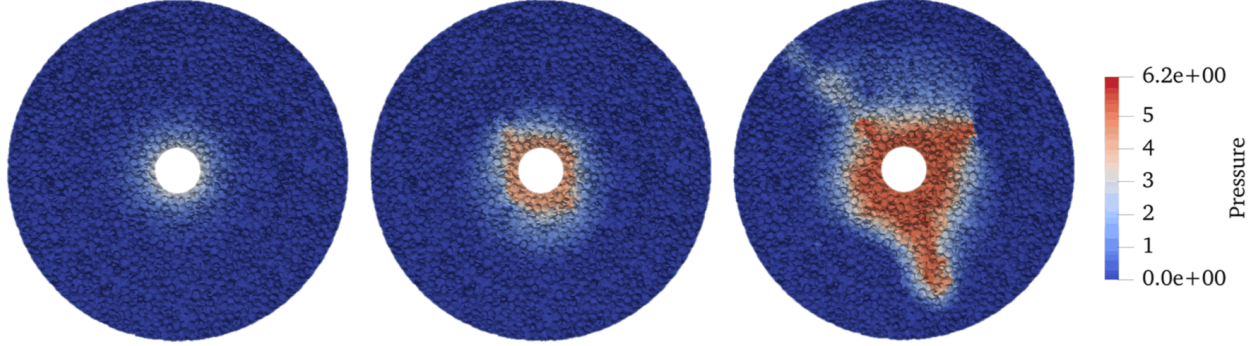


Figure 21: Pore pressure contours for $b = 1.0$ at three moments shown in Fig. 17.

6 Conclusions

This study introduces a comprehensive Multiphysics-Lattice Discrete Particle Model (M-LDPM) framework, specifically formulated for addressing coupled-fracture-poroflow problems in saturated environments. The framework uniquely integrates dual lattice systems: the LDPM tessellation for discrete particle interactions and the Flow Lattice Element (FLE) network for fluid flow simulations. Within this setting, the LDPM governing equations are meticulously adapted to incorporate the effects of fluid pore pressure, while the FLM governing equations for pore pressure flow are derived from mass conservation laws involving both uncracked and cracked volumes. The numerical implementation of the M-LDPM framework is realized through the utilization of Abaqus user element subroutines. A crucial component of the study is the data communication between different solvers facilitated by the Interprocess Communication (IPC), ensuring seamless data exchange and integration of the coupled systems. The framework's technical specifics, and implementation details are thoroughly discussed. Validation of the M-LDPM framework is performed through comparative analyses with analytical solutions of classical poromechanics benchmarks, demonstrating the framework's ability to accurately simulate both one-way and two-way coupling mechanisms with high fidelity. Notably, the M-LDPM results agree exceptionally well with analytical solutions across varying Biot's coefficients and Poisson's ratios for poroelasticity problems. Furthermore, the framework successfully captures the hydraulic fracturing phenomenon, highlighting

the interplay between crack propagation and fluid flow, and underscoring the impact of coupling strength on the material’s load-bearing capacity. Overall, this study establishes the M-LDPM framework as a robust and accurate tool for multiphysics simulations, offering valuable insights and a reliable methodology for exploring complex interactions in saturated poroflow environments.

Acknowledgements

This research was supported in part through the computational resources and staff contributions provided for the Quest high performance computing facility at Northwestern University which is jointly supported by the Office of the Provost, the Office for Research, and Northwestern University Information Technology.

References

- [1] Marina G Alinchenko, Alexey V Anikeenko, Nikolai N Medvedev, Vladimir P Voloshin, Mihaly Mezei, and Pal Jedlovszky. Morphology of voids in molecular systems. a voronoi-delaunay analysis of a simulated dmpc membrane. *The Journal of Physical Chemistry B*, 108(49):19056–19067, 2004.
- [2] Alexey V Anikeenko, MG Alinchenko, VP Voloshin, Nikolai N Medvedev, Marina L Gavrilova, and P Jedlovszky. Implementation of the voronoi-delaunay method for analysis of intermolecular voids. In *Computational Science and Its Applications–ICCSA 2004: International Conference, Assisi, Italy, May 14–17, 2004, Proceedings, Part III* 4, pages 217–226. Springer, 2004.
- [3] Daisuke Asahina, Pengzhi Pan, Kimikazu Tsusaka, Mikio Takeda, and John E Bolan-

- der. Simulating hydraulic fracturing processes in laboratory-scale geological media using three-dimensional tough-rbsn. *Journal of Rock Mechanics and Geotechnical Engineering*, 10(6):1102–1111, 2018.
- [4] Ignatios Athanasiadis, Simon J Wheeler, and Peter Grassl. Hydro-mechanical network modelling of particulate composites. *International Journal of Solids and Structures*, 130:49–60, 2018.
- [5] Maurice A. Biot. General theory of three-dimensional consolidation. *Journal of Applied Physics*, 12(2):155–164, 1941.
- [6] John E Bolander, Jan Eliáš, Gianluca Cusatis, and Kohei Nagai. Discrete mechanical models of concrete fracture. *Engineering Fracture Mechanics*, 257:108030, 2021.
- [7] JE Bolander Jr and Shigehiko Saito. Fracture analyses using spring networks with random geometry. *Engineering Fracture Mechanics*, 61(5-6):569–591, 1998.
- [8] John E Bolander Jr and Stefano Berton. Simulation of shrinkage induced cracking in cement composite overlays. *Cement and Concrete Composites*, 26(7):861–871, 2004.
- [9] Witold Brostow, Mieczyslaw Chybicki, Robert Laskowski, and Jaroslaw Rybicki. Voronoi polyhedra and delaunay simplexes in the structural analysis of molecular-dynamics-simulated materials. *Physical Review B*, 57(21):13448, 1998.
- [10] J William Carey, Zhou Lei, Esteban Rougier, Hiroko Mori, and Hari Viswanathan. Fracture-permeability behavior of shale. *Journal of unconventional oil and gas resources*, 11:27–43, 2015.
- [11] Emanuele Catalano, Bruno Chareyre, and Eric Barthélemy. Pore-scale modeling of fluid-particles interaction and emerging poromechanical effects. *International Journal for Numerical and Analytical Methods in Geomechanics*, 38(1):51–71, 2014.

- [12] Younki Cho, Osman Gonul Apaydin, and Erdal Ozkan. Pressure-dependent natural-fracture permeability in shale and its effect on shale-gas well production. *SPE Reservoir Evaluation & Engineering*, 16(02):216–228, 2013.
- [13] G. Cusatis, A. Mencarelli, D. Pelessone, and J.T. Baylot. Lattice Discrete Particle Model (LDPM) for Failure Behavior of Concrete. II: Calibration and Validation. *Cement and Concrete Composites*, 33(9):891–905, 2011.
- [14] G. Cusatis, D. Pelessone, and A. Mencarelli. Lattice Discrete Particle Model (LDPM) for Concrete failure Behavior of Concrete. I: Theory. *Cement and Concrete Composites*, 33(9):881–890, 2011.
- [15] Catherine A Davy, Frédéric Skoczyłas, J-D Barnichon, and P Lebon. Permeability of macro-cracked argillite under confinement: gas and water testing. *Physics and Chemistry of the Earth, Parts A/B/C*, 32(8-14):667–680, 2007.
- [16] Emmanuel Detournay and Alexander H-D Cheng. Fundamentals of poroelasticity. In *Analysis and design methods*, pages 113–171. Elsevier, 1993.
- [17] Russell L Detwiler. Permeability alteration due to mineral dissolution in partially saturated fractures. *Journal of Geophysical Research: Solid Earth*, 115(B9), 2010.
- [18] Ramsay Dyer, Hao Zhang, and Torsten Möller. Voronoi-delaunay duality and delaunay meshes. In *Proceedings of the 2007 ACM symposium on Solid and physical modeling*, pages 415–420, 2007.
- [19] Jan Eliáš and Gianluca Cusatis. Homogenization of discrete mesoscale model of concrete for coupled mass transport and mechanics by asymptotic expansion. *Journal of the Mechanics and Physics of Solids*, 167:105010, 2022.
- [20] Jan Eliáš, Hao Yin, and Gianluca Cusatis. Homogenization of discrete diffusion models

by asymptotic expansion. *International Journal for Numerical and Analytical Methods in Geomechanics*, 46(16):3052–3073, 2022.

- [21] Jean E Elkhoury, Pasha Ameli, and Russell L Detwiler. Dissolution and deformation in fractured carbonates caused by flow of co₂-rich brine under reservoir conditions. *International Journal of Greenhouse Gas Control*, 16:S203–S215, 2013.
- [22] Caroline Fahy, Simon J Wheeler, Domenico Gallipoli, and Peter Grassl. Corrosion induced cracking modelled by a coupled transport-structural approach. *Cement and Concrete Research*, 94:24–35, 2017.
- [23] Luke P Frash, J William Carey, Zhou Lei, Esteban Rougier, Timothy Ickes, and Hari S Viswanathan. High-stress triaxial direct-shear fracturing of utica shale and in situ x-ray microtomography with permeability measurement. *Journal of Geophysical Research: Solid Earth*, 121(7):5493–5508, 2016.
- [24] William B Fuller and Sanford E Thompson. The laws of proportioning concrete. *Transactions of the American Society of Civil Engineers*, 59(2):67–143, 1907.
- [25] Peter Grassl. A lattice approach to model flow in cracked concrete. *Cement and Concrete Composites*, 31(7):454–460, 2009.
- [26] Peter Grassl and John Bolander. Three-dimensional network model for coupling of fracture and mass transport in quasi-brittle geomaterials. *Materials*, 9(9):782, 2016.
- [27] Peter Grassl, Caroline Fahy, Domenico Gallipoli, and Simon J Wheeler. On a 2d hydro-mechanical lattice approach for modelling hydraulic fracture. *Journal of the Mechanics and Physics of Solids*, 75:104–118, 2015.
- [28] M Gutierrez, LE Øino, and Runar Nygaard. Stress-dependent permeability of a de-mineralised fracture in shale. *Marine and Petroleum Geology*, 17(8):895–907, 2000.

- [29] Leila Hashemi Beni, Mir Abolfazl Mostafavi, Jacynthe Pouliot, and Marina Gavrilova. Toward 3d spatial dynamic field simulation within gis using kinetic voronoi diagram and delaunay tetrahedralization. *International Journal of Geographical Information Science*, 25(1):25–50, 2011.
- [30] Hibbit, Karlsson, and Sorensen. *ABAQUS/CAE user’s manual*. Hibbit, Karlsson & Sorensen, Incorporated, 2002.
- [31] Kunhwi Kim, Jonny Rutqvist, Seiji Nakagawa, and Jens Birkholzer. Tough–rbsn simulator for hydraulic fracture propagation within fractured media: Model validations against laboratory experiments. *Computers & Geosciences*, 108:72–85, 2017.
- [32] Christian Kluge, G Blöcher, H Milsch, Hannes Hofmann, A Nicolas, Z Li, and J Fortin. Sustainability of fractured rock permeability under varying pressure. In *Poromechanics VI*, pages 1192–1199. 2017.
- [33] Leslie Lamport. On interprocess communication: part i: basic formalism. *Distributed computing*, 1:77–85, 1986.
- [34] Scott M Lewandowski. Interprocess communication in unix and windows nt. *Brown University*, page 2, 1997.
- [35] Weixin Li, Faysal Bousikhane, J William Carey, and Gianluca Cusatis. Computational analysis of the fracture-permeability behavior of shale. In *Poromechanics VI*, pages 1200–1207. 2017.
- [36] Weixin Li, Xinwei Zhou, J William Carey, Luke P Frash, and Gianluca Cusatis. Multi-physics lattice discrete particle modeling (m-ldpm) for the simulation of shale fracture permeability. *Rock Mechanics and Rock Engineering*, 51:3963–3981, 2018.
- [37] VA Luchnikov, NN Medvedev, L Oger, and J-P Troadec. Voronoi-delaunay analysis of voids in systems of nonspherical particles. *Physical review E*, 59(6):7205, 1999.

- [38] Bernard Stanford Massey and John Ward-Smith. *Mechanics of fluids*, volume 1. Crc Press, 1998.
- [39] Micaela Mercuri, Madura Pathirage, Amedeo Gregori, and Gianluca Cusatis. Fracturing and collapse behavior of masonry vaulted structures: a lattice-discrete approach. *Procedia Structural Integrity*, 44:1276–1283, 2023.
- [40] Mijo Nikolic, Adnan Ibrahimbegovic, and Predrag Miscevic. Discrete element model for the analysis of fluid-saturated fractured poro-plastic medium based on sharp crack representation with embedded strong discontinuities. *Computer Methods in Applied Mechanics and Engineering*, 298:407–427, 2016.
- [41] Runar Nygård, Marte Gutierrez, Rolf K Bratli, and Kaare Høeg. Brittle–ductile transition, shear failure and leakage in shales and mudrocks. *Marine and Petroleum Geology*, 23(2):201–212, 2006.
- [42] César Luiz Palagi and Khalid Aziz. Use of voronoi grid in reservoir simulation. *SPE Advanced Technology Series*, 2(02):69–77, 1994.
- [43] James R Rice and Michael P Cleary. Some basic stress diffusion solutions for fluid-saturated elastic porous media with compressible constituents. *Reviews of Geophysics*, 14(2):227–241, 1976.
- [44] Martin Robinson, Marco Ramaoli, and Stefan Luding. Fluid–particle flow simulations using two-way-coupled mesoscale sph–dem and validation. *International journal of multiphase flow*, 59:121–134, 2014.
- [45] John W Rudnicki. Fluid mass sources and point forces in linear elastic diffusive solids. *Mechanics of materials*, 5(4):383–393, 1986.
- [46] J Rutqvist, JT Birkholzer, and Chin-Fu Tsang. Coupled reservoir–geomechanical analysis of the potential for tensile and shear failure associated with co₂ injection in multilay-

- ered reservoir–caprock systems. *International Journal of Rock Mechanics and Mining Sciences*, 45(2):132–143, 2008.
- [47] Lei Shen, Weixin Li, Xinwei Zhou, Jun Feng, Giovanni Di Luzio, Qingwen Ren, and Gianluca Cusatis. Multiphysics lattice discrete particle model for the simulation of concrete thermal spalling. *Cement and Concrete Composites*, 106:103457, 2020.
- [48] Lei Shen, Huayi Zhang, Giovanni Di Luzio, Hao Yin, Lifu Yang, and Gianluca Cusatis. Mesoscopic discrete modeling of multiaxial load-induced thermal strain of concrete at high temperature. *International Journal of Mechanical Sciences*, 232:107613, 2022.
- [49] Kun Su, Y Sanz Perl, Atef Onaisi, Hamid Pourpark, and Sandrin Vidal-Gilbert. Experimental study of hydromechanical behavior of fracture of vaca muerta gas shale. In *ARMA US Rock Mechanics/Geomechanics Symposium*, pages ARMA–2017. ARMA, 2017.
- [50] Ole Ivar Ulven and WaiChing Sun. Capturing the two-way hydromechanical coupling effect on fluid-driven fracture in a dual-graph lattice beam model. *International Journal for Numerical and Analytical Methods in Geomechanics*, 42(5):736–767, 2018.
- [51] Vladimir P Voloshin, Alexandra V Kim, Nikolai N Medvedev, Roland Winter, and Alfons Geiger. Calculation of the volumetric characteristics of biomacromolecules in solution by the voronoi–delaunay technique. *Biophysical Chemistry*, 192:1–9, 2014.
- [52] K von Terzaghi. Die berechnung der durchassigkeitsziffer des tones aus dem verlauf der hydrodynamischen spannungs. erscheinungen. *Sitzungsber. Akad. Wiss. Math. Naturwiss. Kl. Abt. 2A*, 132:105–124, 1923.
- [53] Kun Wang and WaiChing Sun. A semi-implicit discrete-continuum coupling method for porous media based on the effective stress principle at finite strain. *Computer Methods in Applied Mechanics and Engineering*, 304:546–583, 2016.

- [54] Paul Adams Witherspoon, Joseph SY Wang, K Iwai, and John E Gale. Validity of cubic law for fluid flow in a deformable rock fracture. *Water resources research*, 16(6):1016–1024, 1980.
- [55] Lifu Yang, Kai Li, Xiang Hu, Zesen Peng, Qing-feng Liu, and Caijun Shi. Mesoscopic discrete modeling of compression and fracture behavior of concrete: Effects of aggregate size distribution and interface transition zone. *Cement and Concrete Composites*, 147:105411, 2024.
- [56] Lifu Yang, Madura Pathirage, Huaizhi Su, Mohammed Alnaggar, Giovanni Di Luzio, and Gianluca Cusatis. Computational modeling of temperature and relative humidity effects on concrete expansion due to alkali–silica reaction. *Cement and Concrete Composites*, 124:104237, 2021.
- [57] IW Yeo, MH De Freitas, and RW Zimmerman. Effect of shear displacement on the aperture and permeability of a rock fracture. *International journal of rock mechanics and mining sciences*, 35(8):1051–1070, 1998.
- [58] Hao Yin, Antonio Cibelli, Susan-Alexis Brown, Lifu Yang, Lei Shen, Mohammed Alnaggar, Gianluca Cusatis, and Giovanni Di Luzio. Flow lattice model for the simulation of chemistry dependent transport phenomena in cementitious materials. *European Journal of Environmental and Civil Engineering*, pages 1–25, 2023.
- [59] Robert W Zimmerman and Gudmundur S Bodvarsson. Hydraulic conductivity of rock fractures. *Transport in porous media*, 23:1–30, 1996.